MATEMATICKO-FYZIKÁLNÍ
FAKULTA
Univerzita Karlova

DIPLOMOVÁ PRÁCE

Zuzana Jelínková

Studium vlastností neutrin pomocí NOvA detektoru

Ústav částicové a jaderné fyziky

Vedoucí diplomové práce:	RNDr. Karel Soustružník, Ph.D.
Studijní program:	Fyzika
Studijní obor:	Jaderná a subjaderná fyzika

Praha 2017

FACULTY
OF MATHEMATICS
AND PHYSICS
Charles University

MASTER THESIS

Zuzana Jelínková

Study of neutrino properties using NOvA detector

Institute of Particle and Nuclear Physics

Supervisor of the master thesis:	RNDr. Karel Soustružník, Ph.D.
Study programme:	Physics
Study branch:	Nuclear and Subnuclear Physics

Prague 2017

I declare that I carried out this master thesis independently, and only with the cited sources, literature and other professional sources.

I understand that my work relates to the rights and obligations under the Act No. 121/2000 Sb., the Copyright Act, as amended, in particular the fact that the Charles University has the right to conclude a license agreement on the use of this work as a school work pursuant to Section 60 subsection 1 of the Copyright Act.

In .... date .... signature of the author

Název práce: Studium vlastností neutrin pomocí NOvA detektoru

Autor: Zuzana Jelínková

Katedra: Ústav částicové a jaderné fyziky

Vedoucí diplomové práce: RNDr. Karel Soustružník, Ph.D.

Abstrakt: Experiment NOνA se zabývá oscilacemi neutrin a patří mezi experimenty s dlouhou oscilační dráhou. Je navržen na měření elektronových neutrin objevujících se v NuMI svazku, zdroji mionových neutrin ve Fermilabu. Oba detektory NOνy, Blízký a Vzdálený, jsou funkčně identické aktivní dráhové kalorimetry. Zaměřením této diplomové práce je relativní kalibrace Blízkého Detektoru. Popsány jsou jednotlivé kroky procesu: prahová, stínová a útlumová kalibrace. NOνA standardně používá na kalibraci kosmické miony. Představen je alternativní zdroj, tzv. miony ze skály, které vznikají interakcemi mionových neutrin ze svazku ve skále obklopující Blízký Detektor. Práce provádí jednotlivými kroky vývoje selekčních kritérií, pomocí kterých jsou z dat vybírány dráhy mionů ze skály. Takto vybraný vzorek drah mionů ze skály je použit na relativní kalibraci a výsledky každého kroku jsou následně porovnány s relativní kalibrací provedenou kosmickými miony. K vypracování analýzy v této práci byla využita simulovaná data.

Klíčová slova: neutrina, oscilace, NOνA, kalibrace

Title: Study of neutrino properties using NOvA detector

Author: Zuzana Jelínková

Department: Institute of Particle and Nuclear Physics

Supervisor: RNDr. Karel Soustružník, Ph.D.

Abstract: The NOνA experiment is a long-baseline neutrino oscillation experiment designed to measure electron neutrinos (ν_e) appearing in the NuMI beam, a muon neutrino (ν_μ) source at Fermilab. Its two detectors, Near and Far, are functionally identical active tracking calorimeters. This thesis is focused on the relative calibration of the Near Detector. The individual steps of the process, threshold, shadowing and attenuation calibration, are described. For the calibration, NOνA standardly uses cosmic muons. Alternative source, so called rock muons which are muons that originated from interactions of beam ν_μs with a rock surrounding the Near Detector, is introduced. The thesis guides through the development of selection criteria used to distinguish rock muon tracks from the data. Selected sample of rock muon tracks is used for the relative calibration and at each step the results are compared to the cosmic muons based calibration. The whole analysis is performed using simulated Monte Carlo data.

Keywords: neutrino, oscillations, NOνA, calibration

There is quite a number of people who kindly provided me with their support in various forms. Each and every one of those was essential. All of them gave me a piece to a mosaic I needed to make this thesis happen.

In the first place I'd like to thank my supervisor Karel Soustružník who introduced me to the fascinating NOνA experiment and gave me the matchless opportunity to visit Fermilab, the place where it all happens. Many amazing and smart people I'll mention further I've met right there.

My greatest gratitude goes to Brian Rebel, at the time convener of the Calibration group at NOνA. Brian was the one who had the idea of using rock muons to calibrate the Near Detector in mind and put his trust in me to commence this task. He would answer all my questions and patiently explain everything I needed to know. He was an irreplacable mentor to me, I learned a great lot from him.

I couldn't even start with the actual analysis if not for Kanika Sachdev and Evan Niner. They led me by the hand and taught me how to write new and edit an existing code in NOνA software. They gave me the foundations of the way the analysis is done at NOνA focusing on the goal I wanted to achieve. I can not thank them enough for investing their precious time in me.

On the same level I want to express my appreciation to Prabhjot Singh. Prabhjot provided me with all the necessary calibration scripts, explained to me how to use them and also wrote some especially for my needs. If I got stuck he would never let me without solving the problem. He was always ready to consult any issues with me.

Another amazing people I met in Fermilab are Daisy Karla and Nitin Yadav. They granted me with the most important thing — friendship. I am very grateful for spending their time with me, teaching me Hindi and sharing delicious Indian food with me. Also, they would never hesitate to share their experience about the NOνA experiment as well.

It took me a while to finish this thesis. The one who suffered because of it the most is my boss at Jumpshot, Martin Mesršmíd. Any time I needed a longer time off to work on the thesis he would approve anyway. Therefore, my special thanks goes right to him.

The struggle with the formal visage of the thesis broke my colleague Břetislav Šopík. I found in him an expert on writing the science articles with his many years of experience in academic field. He taught me all the rules of how the professional written word should look like. I greatly appreciate the time and energy he devoted to me.

I am also obliged to my schoolmate and NOνA colleague Tomáš Nosek. He helped me capture all the factual and formal discrepancies I wouldn't realize I had.

For taking off all responsibilites of me so that I could focus on work I thank my boyfriend, Mikuláš Valeš. He's been taking care of me as noone else ever did.

I'd like to thank my family, too, for unconditional love and support.

Contents

Introduction

The NOνA experiment uses two fine grained detectors to measure the properties of the particles called neutrinos. The Near Detector is located in the underground cavern at FNAL and the Far Detector is located near the Ash River, MN, 810 km away from the Near Detector. The source of the neutrinos for the NOνA experiment is the NuMI beam of ν_μs 1 km away from the Near Detector. Currently, both detectors are calibrated using cosmic muons originating from collisions of cosmic rays with the nuclei in the atmosphere. However, in the Near Detector there is another source of muons, so called rock muons, present that could be used for the calibration as well. The rock muons originate from the interactions of beam neutrinos with the nuclei in the rock surrounding the Near Detector. In this thesis we compare the use of cosmic muons and rock muons in terms of the relative calibration of the Near Detector. Analyzed were the simulated data with the idea of extending these steps to real data situation in mind.

In the first chapter neutrinos and their oscillations are briefly introduced together with the current knowledge of values of the oscillation parameters. In the second chapter the motivation behind and a basic design features of the NOνA experiment are presented. The third chapter contains a description of the individual steps of the relative calibration process. The fourth chapter guides through the development of the criteria selecting sufficiently pure sample of rock muons by applying conditions on the reconstructed variables. The final chapter presents the rock and cosmic muons sample comparisons of the variables entering the relative calibration calculation. The influence of individual specifics of both types of muons to these variables is discussed. Finally, the performance of the relative calibration using cosmic and rock muons is compared.

The calibration of the detector response has a significant share in a systematic error in the NOνA analyses. This thesis aims to validate the current calibration method with the independent set of events while breaking it down to individual steps and study the specificities of each of the muon sources.

1. Neutrinos

Neutrinos are electrically neutral elementary particles described by the Standard Model which interact only with the weak interaction. They are very difficult to detect but not as impossible as it was presumed at first. The very idea of neutrino-like particle, at the time called neutron, was proposed by Wolfgang Pauli in often mentioned letter to the Tubingen physics conference in 1930 as a possible explanation of continuous β spectrum in β-decay experiments without violating the conservation of energy. In 1934 Enrico Fermi built the first theory of nuclei β-decay based on Pauli's idea that in the β-decay an electrically neutral, spin 1/2 and very light particle is emitted together with an electron [1]. Since the heavy neutron was meanwhile discovered, Fermi decided to call the elusive particle as a little brother to neutron — neutrino. Sixty years later, in 1995, Frederick Reines received a Nobel prize for successful detection of this elusive particle in an experiment based on inversed β-decay which he performed in 1956 with his colleague Clyde L. Cowan [2].

By the current knowledge there are three types — flavours — of neutrinos, called by the corresponding lepton family — electron neutrino (ν_e), muon neutrino (ν_μ) and tau neutrino (ν_τ). Each neutrino has its antiparticle called antineutrino — $\bar{\nu}_e$, $\bar{\nu}_\mu$, $\bar{\nu}_\tau$. The neutrino which is produced with a lepton l^+ (l^-) or produces an l^- (l^+) in weak charged-current (CC) interaction is noted as ν_l ($\bar{\nu}_l$). For the case when $l = e$ the neutrino (antineutrino) is noted as ν_e ($\bar{\nu}_e$), *etc.* However, when a neutrino with a specific flavour is produced it can subsequently interact as a neutrino of a different flavour. Such events are known as neutrino oscillations and can occur with a certain probability.

The first conceptual idea of oscillating neutrinos came from Bruno Pontecorvo in 1957. He was looking for a process in lepton world analoguous to $K^0 \to \bar{K}^0$ transition [3]. The first experimental indication of neutrino oscillations was the so called “Solar neutrino problem”. The resulting counts of neutrinos in Davis Homestake experiment designed to detect ν_es from the Sun were only 1/3 of the amount predicted by the Bahcall's Standard Solar Model. Explanation was that missing 2/3 of ν_es oscillated on a way to detector into ν_μs or ν_τs and thus weren't detected.

1.1 Neutrino mixing and oscillations

Oscillations of neutrinos are a consequence of the presence of flavour neutrino mixing, or lepton mixing, in vacuum [4]. By the flavour neutrino mixing we mean that a state of defined neutrino flavour can be expressed as the linear combination of mass eigenstates:

$$|\nu_\alpha\rangle = \sum_{k=1}^{3} U^*_{\alpha k} \, |\nu_k\rangle \, , \quad \alpha = e, \mu, \tau, \tag{1.1}$$

where U is the 3×3 unitary matrix known as Pontecorvo-Maki-Nakagawa-Sakata (PMNS) mixing matrix [5], $|\nu_\alpha\rangle$ represent the flavour eigenstates and $|\nu_k\rangle$ mass eigenstates. The PMNS matrix in one of its typical forms reads:

$$U = \begin{pmatrix} 1 & 0 & 0 \\ 0 & c_{23} & s_{23} \\ 0 & -s_{23} & c_{23} \end{pmatrix} \begin{pmatrix} c_{13} & 0 & s_{13}e^{-i\delta} \\ 0 & 1 & 0 \\ -s_{13}e^{i\delta} & 0 & c_{13} \end{pmatrix} \begin{pmatrix} c_{12} & s_{12} & 0 \\ -s_{12} & c_{12} & 0 \\ 0 & 0 & 1 \end{pmatrix} \times \begin{pmatrix} e^{i\alpha_1/2} & 0 & 0 \\ 0 & e^{i\alpha_2/2} & 0 \\ 0 & 0 & 1 \end{pmatrix}. \tag{1.2}$$

After evaluating the first three matrices we obtain:

$$U = \begin{pmatrix} c_{13}c_{12} & c_{13}s_{12} & s_{13}e^{-i\delta} \\ -c_{13}s_{12} - s_{13}s_{23}c_{12}e^{-i\delta} & c_{23}c_{12} - s_{13}s_{23}s_{12}e^{-i\delta} & c_{13}s_{23} \\ s_{23}s_{12} - s_{13}c_{23}c_{12}e^{-i\delta} & -s_{23}c_{12} - s_{13}c_{23}s_{12}e^{-i\delta} & c_{13}c_{23} \end{pmatrix} \times \begin{pmatrix} e^{i\alpha_1/2} & 0 & 0 \\ 0 & e^{i\alpha_2/2} & 0 \\ 0 & 0 & 1 \end{pmatrix}, \tag{1.3}$$

where $c_{ij} = \cos\theta_{ij}$ and $s_{ij} = \sin\theta_{ij}$. Parameters θ_{ij} are so called mixing angles, parameter δ is called the Dirac CP violation phase and parameters α_1 and α_2 are called the Majorana CP violation phases. Majorana phases do not have any effect in the neutrino oscillation process [6], therefore they are left from further elaboration. The probability that neutrino of energy E [GeV] with former flavour α will be detected with a flavour β after passing a distance L [km] in vacuum is [7]:

$$P(\nu_\alpha \longrightarrow \nu_\beta) = \delta_{\alpha\beta} - 4\sum_{i>j=1}^{3} \mathrm{Re}(K_{\alpha\beta,ij})\sin^2\left(\frac{\Delta m_{ij}^2 L}{4E}\right) + 4\sum_{i>j=1}^{3} \mathrm{Im}(K_{\alpha\beta,ij})\sin\left(\frac{\Delta m_{ij}^2 L}{4E}\right)\cos\left(\frac{\Delta m_{ij}^2 L}{4E}\right), \tag{1.4}$$

where

$$K_{\alpha\beta,ij} = U_{\alpha i}U_{\beta i}^{*}U_{\alpha j}^{*}U_{\beta j}. \tag{1.5}$$

From the formula it is obvious that the probability depends on parameters of the PMNS matrix, ratio of the propagation distance to the initial neutrino energy L/E and the mass squared differences of individual mass eigenstates $\Delta m_{ij}^2 \equiv (m_j^2 - m_i^2), i \not\equiv j$. We also easily see that for oscillations to occur neutrino mass eigenstates must differ in their masses so that Δm_{ij}^2 is not zero. Since the probability is sensitive only to the squared mass difference it is impossible to determine the absolute value of masses from the oscillation experiments.

1.2 Current status of oscillation parameters

In general, the oscillation probabilities are governed by 6 oscillation parameters that need to be experimentaly obtained: mixing angles θ_{12}, θ_{13}, θ_{23}, CP violation phase δ and mass squared differences from which only two are independent, say Δm_{21}^2 and Δm_{31}^2, where $|\Delta m_{31}^2| - |\Delta m_{21}^2| = |\Delta m_{32}^2|$. It's been already determined that $m_1^2 < m_2^2$ and $\Delta m_{21}^2 > 0$. The experimental results show the value $\Delta m_{21}^2 = (7.53 \pm 0.18) \times 10^{-5}$ eV^2 [4]. This value is small with respect to either $|\Delta m_{31}^2|$ or $|\Delta m_{32}^2|$, see Table 1.1. This fact allows for approximation $|\Delta m_{31}^2| \approx |\Delta m_{32}^2|$ in neutrino oscilllations probability formulas [8]. However, the sign of the Δm_{31}^2 is yet to be determined. The state of $\Delta m_{31}^2 > 0$ when the ordering of neutrino masses is $m_3^2 > m_2^2 > m_1^2$ is called the Normal mass hierarchy (NH) and the state of $\Delta m_{31}^2 < 0$ with $m_2^2 > m_1^2 > m_3^2$ is called the Inverted mass hierarchy (IH). A scheme of the mass hierarchies is shown in Fig. 1.1.

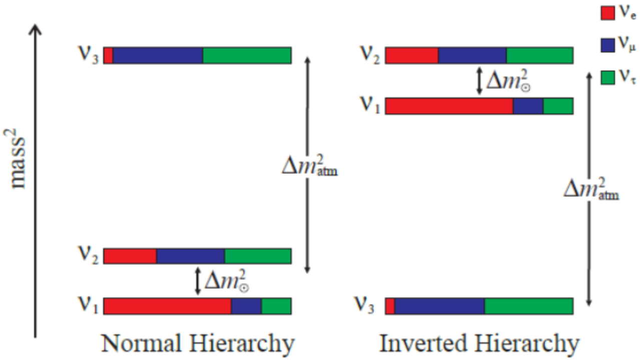

Figure 1.1: The scheme of the mass hierarchies. Ordering of the neutrino mass eigenstates masses with ν_3 being the heaviest is called the Normal hierarchy while the Inverted hierarchy is called the ordering with ν_3 being the lightest. It is yet to be discovered which of these two hierarchies actually realizes in nature. Figure was taken from [9].

The parameters Δm_{21}^2 and θ_{12} are often called "solar" and denoted as $\Delta m_\odot^2$ and $\theta_\odot$ since their values are associated with oscillations of ν_es coming from the Sun. Their current best estimate values can be found in Table 1.1 and have been researched by solar neutrino experiments such as SAGE, GALLEX, Super-Kamiokande and SNO as well as by the experiment KamLAND studying $\bar{\nu}_e$s from the nuclear reactor.

The parameters Δm_{32}^2 and θ_{23} are often called "atmospheric" and denoted as $\Delta m_{\rm atm}^2$ and $\theta_{\rm atm}$. Their values have dominant effect on oscillations of ν_μ and $\bar{\nu}_\mu$ created by collisions of cosmic rays with the nuclei in the atmosphere. Their current best estimate values can be found in Table 1.1. The value of θ_{23} is still determined with a relatively large uncerainty. It's close to $\pi/4$ but the octant, whether it's $> 45°$ or $< 45°$ or $= 45°$, is still at the moment unresolved. Atmospheric parameters have been studied in long-baseline neutrino experiments ($L \sim 100 - 1000$ km) such as K2K, MINOS, T2K and NOνA which is described more in the following section.

On measurement of θ_{13} are focused reactor $\bar{\nu}_e$ disappearance experiments with short-baseline ($L \sim 1$ km) such as RENO, Double Chooz and Daya Bay. The global fit of the θ_{13} can be found in Table 1.1. The most precise measurement up to date is from the Daya Bay experiment with the result of $\sin^2 2\theta_{13} = 0.084 \pm 0.005$ eV^2 [10].

With $\theta_{13} \neq 0$, the Dirac phase δ can generate CP violating effects in neutrino oscillations, *i.e.* a difference between the probabilities of the $\nu_l \rightarrow \nu_{l'}$ and $\bar{\nu}_l \rightarrow \bar{\nu}_{l'}$,

$l \neq l' = e, \mu, \tau$. However, the current experimental data does not significantly constrain the parameter δ [11].

Table 1.1: The best currently known values of neutrino oscillations parameters for Normal Hierarchy (NH) and Inverted Hierarchy (IH) [4].

Parameter	value
$\sin^2\theta_{12}$	0.304 ± 0.014
Δm^2_{21}	$(7.53 \pm 0.18) \times 10^{-5}$ eV^2
$\sin^2\theta_{23}$ (NH)	0.51 ± 0.05
$\sin^2\theta_{23}$ (IH)	0.50 ± 0.05
Δm^2_{32} (NH)	$(2.44 \pm 0.06) \times 10^{-3}$ eV^2
Δm^2_{32} (IH)	$(2.51 \pm 0.06) \times 10^{-3}$ eV^2
$\sin^2\theta_{13}$	$(2.19 \pm 0.12) \times 10^{-2}$

2. The NOνA Experiment

Acronym NOνA stands for **N**uMI **O**ff-Axis ν_e **A**ppearance. The purpose of the NOνA experiment is to measure the electron neutrinos appearing oscillated from a muon neutrino NuMI (Neutrinos at the Main Injector) beam as well as the decrease of the ν_μ flux due to the oscillations. Used are two detectors, Near and Far, located 14 mrad off the beam axis with the 810 km distance between them. The angle of 14 mrad was chosen because the energy spectrum of neutrinos has relatively narrow peak at 2 GeV in this composition. This in combination with 810 km distance maximizes sensitivity to the mass ordering resolution and observation of CP violation effects [12]. See Fig. 2.1 for neutrino energy spectra in different positions of detectors and $\nu_\mu \to \nu_e$ oscillation probability as a function of neutrino energy for the 810 km distance between detectors.

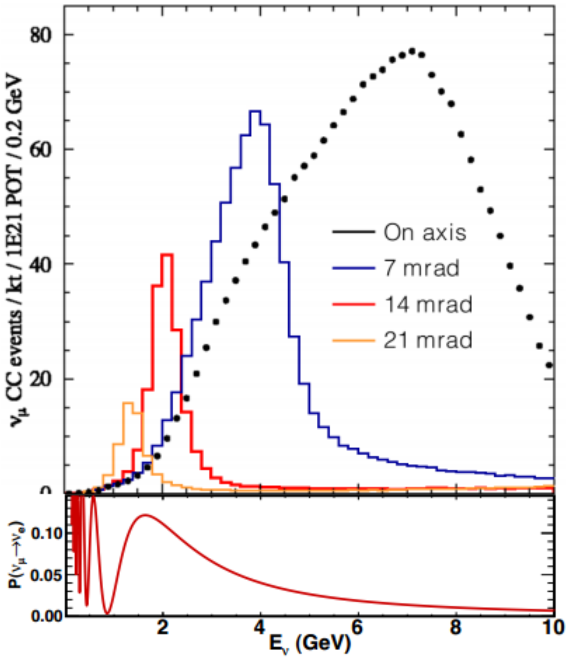

Figure 2.1: **Top**: Energy spectrum of CC ν_μ event rates prior to oscillations for different off-axis positions of detector at the distance of 810 km from Fermilab. NOνA's detectors position is at 14 mrad with respect to the beam axis. **Bottom**: Plot shows the $\nu_\mu \to \nu_e$ oscillation probability as a function of neutrino energy for the 810 km distance between detectors. NOνA's neutrino energy spectrum peaked at 2 GeV is close to local maxima of this probability. Figure was taken from [13].

2.1 Neutrino oscillations at the NOνA experiment

Two main analysis channels that the NOνA experiment focuses on are the ν_μ disappearance and the ν_e apperance channel. The ν_μ disappearance channel is exploring the survival probability $P(\nu_\mu \to \nu_\mu)$ of ν_μ being detected as ν_μ. The ν_e apperance channel studies the probability $P(\nu_\mu \to \nu_e)$ of $\nu_\mu \to \nu_e$ transition. Let us first focus on the latter process which in vacuum is described by a formula:

$$P(\nu_\mu \to \nu_e) \approx P_{\text{atm}} + P_{\text{sol}} + 2\sqrt{P_{\text{atm}}P_{\text{sol}}}[\cos\Delta_{23}\cos\delta \mp \sin\Delta_{32}\sin\delta], \tag{2.1}$$

with

$$P_{\text{atm}} \equiv \sin^2\theta_{23}\sin^2 2\theta_{13}\sin^2\Delta_{31}, \tag{2.2}$$

and

$$P_{\text{sol}} \equiv \cos^2\theta_{23}\cos^2\theta_{13}\sin^2 2\theta_{12}\sin^2\Delta_{21} \approx \cos^2\theta_{23}\cos^2\theta_{13}\sin^2 2\theta_{12}\Delta_{21}^2, \tag{2.3}$$

where $\Delta_{ij} \equiv \Delta m_{ij}^2 L/2E$ and the $\mp$ in Eq. (2.1) is the negative sign for neutrinos and the positive sign for antineutrinos. The derivation of this formula is indicated in [8]. Neutrinos from the NuMI beam are not travelling through the vacuum, though. They travel from their source to the Far Detector through the Earth. The fact that neutrinos can interact with particles of matter is modifying the oscillation probabilities. This modification is generally called a “matter effect”. Contributing interaction for ν_e is a coherent forward elastic weak charged-current scattering with electrons and for all neutrino flavours a neutral-current scattering with electrons, protons and neutrons present in the matter. See Feynman diagrams of these interactions in Fig. 2.2 [14].

Inequality in charged-current scattering for ν_e versus that for ν_μ and ν_τ may create significant enhancement or suppression of oscillation probabilities for high matter density environment such as star cores but can also be crucial in less dense environments such as Earth crust. With the matter effect the terms P_{atm} and P_{sol} in $P(\nu_\mu \to \nu_e)$ are modified as follows:

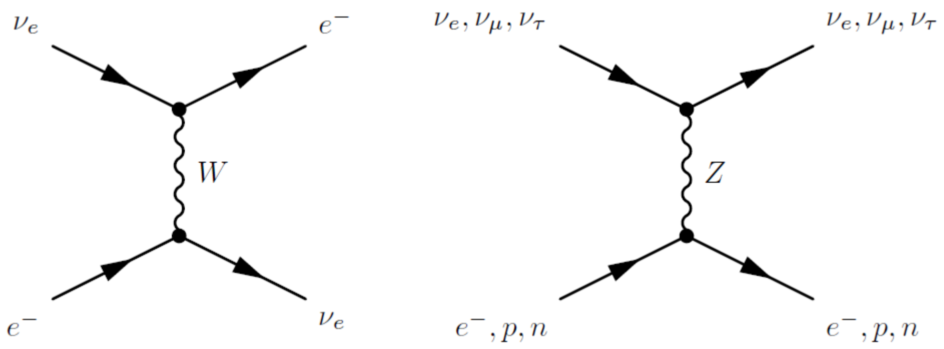

Figure 2.2: **Left:** Feynman diagram of charged-current (CC) scattering. **Right:** Feynman diagram of neutral-current (NC) scattering. CC mediated by charged W bosons can occur only for ν_e scattering on electrons since normal matter does not contain μ or τ. This creates a possibility for significant enhancement or suppression of oscillation probabilites. NC mediated by Z bosons is flavour-blind which means that neutrino with any flavour can interact through it with any matter particle, e^-, p, n. Figure was taken from [14].

$$P_{\text{atm}} = \sin^2\theta_{23}\sin^2 2\theta_{13}\frac{\sin^2(\Delta_{31} \mp aL)}{(\Delta_{31} \mp aL)^2}\Delta_{31}^2, \tag{2.4}$$

and

$$P_{\text{sol}} = \cos^2\theta_{23}\sin^2 2\theta_{12}\frac{\sin^2(\mp aL)}{(\mp aL)^2}\Delta_{21}^2, \tag{2.5}$$

where $a \equiv G_F N_e/\sqrt{2}$, G_F is the Fermi constant and N_e is the matter electron number density. The $\mp$ in Eq. (2.4) and Eq. (2.5) is again negative sign for neutrinos and positive sign for antineutrinos. For the baseline value of the NOνA experiment $L = 810$ km the term $aL \approx 0.23$ which makes the matter effect significant for the ν_e appearance channel [8]. The illustration of the differences in $P(\nu_\mu \to \nu_e)$ for ν and $\bar{\nu}$ and NH and IH due to the matter effect in the NOνA case ($L = 810$ km) assuming $\delta_{\text{CP}} = 0$ is depicted in Fig. 2.3.

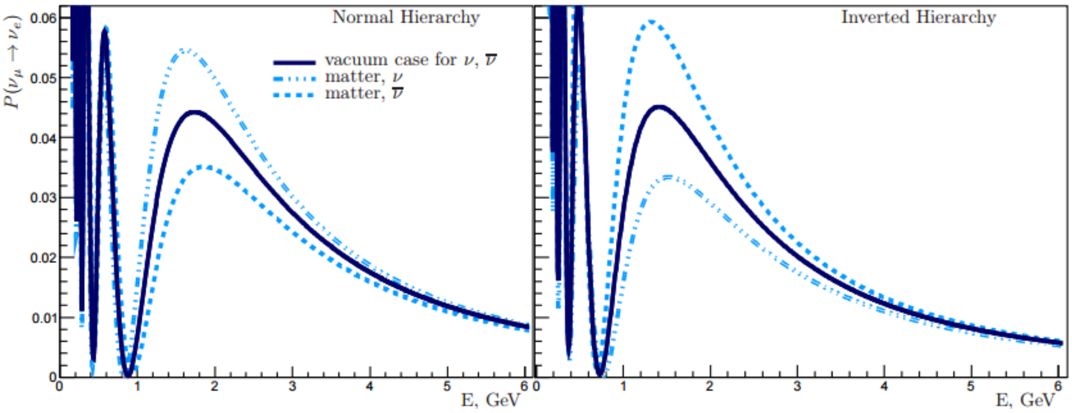

Figure 2.3: Illustration of the matter effect on the oscillation probability $P(\nu_\mu \to \nu_e)$ as a function of energy in the NOνA case ($L = 810$ km) assuming $\delta_{\text{CP}} = 0$. **Left:** Normal hierarchy. **Right:** Inverted hierarchy. The probability for ν and $\bar{\nu}$ splits due to different signs in Eq. (2.4) and Eq. (2.5). For NH the ν probability is enhanced while the $\bar{\nu}$ is suppressed and vice versa for IH. Figure was taken from [15].

The NuMI beam has a capability of changing the beam from ν_μ to beam of $\bar{\nu}_\mu$. Thus it will be possible to compare the measured $P(\nu_\mu \to \nu_e)$ and $P(\bar{\nu}_\mu \to \bar{\nu}_e)$, *i.e.* in practice, compare the counts of detected $\nu_\mu \to \nu_e$ events and $\bar{\nu}_\mu \to \bar{\nu}_e$ events. By fitting these measurements to the Eqs. 2.1, 2.4 and 2.5 we can get insight to the value of δ, the octant of θ_{23} and the mass ordering.

Let us now focus on the process of ν_μ disappearance. Its probability in vacuum has a form [8]:

$$P(\nu_\mu \to \nu_\mu) \approx 1 - \sin^2 2\theta_{23}\sin^2\Delta_{23}. \tag{2.6}$$

In ν_μ disappearance channel the matter effect in case of the L and E setting of the NOνA experiment has a value $< 1\%$ and thus can be neglected in the $P(\nu_\mu \to \nu_\mu)$ formula [8]. The ν_μ disappearance analysis is performed by measuring the oscillated energy spectrum of the ν_μ at the Far Detector. The measured energy spectrum is then compared to the simulated energy spectra with different settings of parameters $\sin^2\theta_{23}$ and Δm_{23}^2. The simulated spectrum that fits best the measured spectrum then yields the values of the actual $\sin^2\theta_{23}$ and Δm_{23}^2 parameters.

To summarize, the physics goals of NOνA experiment are following:

- Resolve octant of θ_{23} or determine if it is maximal.
- Get some insight into mass ordering — the sign of Δm^2_{32}.
- Measure the value of $|\Delta m^2_{32}|$.
- Discover or constrain the value of the parameter δ — the amount of CP violation in neutrino sector.

In the February 2017 ended the period of the neutrino mode ($\nu_\mu \rightarrow \nu_\mu, \nu_\mu \rightarrow \nu_e$) which was on for 3 years (since Feb 2014). The NuMI beam is now set to the antineutrino mode ($\bar{\nu}_\mu \rightarrow \bar{\nu}_\mu, \bar{\nu}_\mu \rightarrow \bar{\nu}_e$) and is planned to run for another 3 years with expected end at the turn of 2020 and 2021.

2.2 NuMI Beam

Neutrino source for the NOνA experiment is NuMI (Neutrinos at the Main Injector) beamline at Fermilab. For the purposes of the NOνA experiment NuMI has been upgraded from the former power 300 kW to the current 700 kW. The NuMI beam is created by directing 120 GeV protons from the Main Injector to the fixed graphite target. The secondary beam of charged pions and kaons is focused by two parabolic magnetic horns. By changing the polarity of horns it is possible to select either positively or negatively charged mesons with the end product of predominantly neutrino or anti-neutrino beam respectively. Focused beam of kaons and pions is lead to 675 m long and 2 m in diameter evacuated decay pipe. Here mesons decay producing charged leptons and neutrinos. Decay pipe is followed by aluminium hadron absorber, three ionization chambers to monitor outgoing muons interspersed with total of 240 m of rock ensuring the final pure neutrino beam [13, 16, 17]. For the schema of described NuMI beam production see Fig. 2.4.

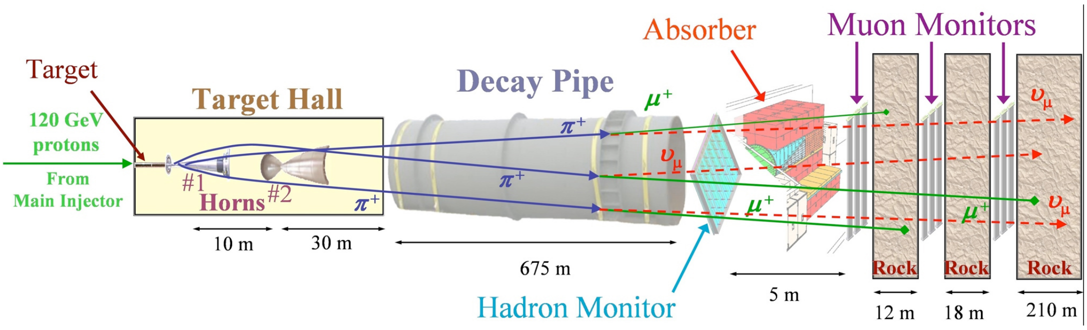

Figure 2.4: NuMI beam production. See description in text. Figure was taken from [17].

2.3 NOνA Detectors

The NOνA experiment uses two functionally identical detectors, one smaller located 1 km from the beam source in the cavern in Fermilab called Near Detector

(ND) and other, bigger, 810 km away in Minnesota known as Far Detector (FD). ND's position close to the beam source allows for accurate description of beam's composition so that it can be precisely compared to what FD sees 810 km away. Detectors are both active tracking calorimeters with fine-grained structure specifically designed to well distinguish electromagnetic showers caused by electrons. That is crucial for the experiment as electrons are the product of electron neutrinos signal charged current interactions. Specificities for each of the detectors are in the Subsection 2.3.2 for the ND and in the Subsection 2.3.3 for the FD.

2.3.1 Basic Detector unit

A basic structure unit of the detectors is an extruded PVC cell 3.9 cm wide and 5.9 cm deep filled with a low-Z liquid scintillator. Each cell has a loop of 0.7 milimeter thick wavelength-shifting fiber in it to catch the scintillation light. The fiber goes through the whole length of the cell which is for ND 4 m and FD 16 m making a light attenuation a significant effect that has to be corrected for.

Inner walls of the cell are covered with a highly reflective titanium dioxide. Charged particles traverse the cell creating a light in the liquid scintillator. The light is then bounced off the walls until it's captured by the fiber or absorped by the PVC or the scintillator. See Fig. 2.5 left for a scheme of the cell. The wavelength-shifting fiber leads the captured light towards its two ends both connected to one pixel of Avalanche Photo-Diode (APD) chip. One APD chip has 32 pixels collecting light from 32 cells. See Fig. 2.5 right showing the APD chip next to a penny. Using the photoelectric effect in the APD the optical signal is converted to the electronic signal. It is read out by the front-end board (FEB)

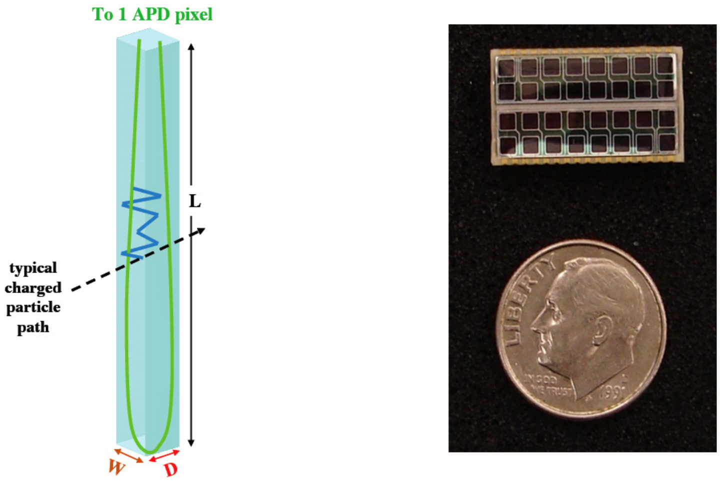

Figure 2.5: **Left**: Extruded PVC cell with W = 3.9 cm and D = 5.9 cm filled with a liquid scintillator and looped wavelength-shifting fiber. The interaction of charged particle passing through the cells produces a light in the scintillator (blue track) which is reflected off the cell walls until it is absorbed by the wavelength-shifting fiber. Fiber leads the light to the APD. **Right**: 32 channel avalanche photo-diode next to a penny. Two ends of the optical fiber lead to one APD chip pixel. Figures taken from [17].

where the signal is time stamped and shaped. On the FEB there is an analog-to-digital converter (ADC) which digitalizes the analog signal from the APD. If the hit is above threshold it is lead from the FEB to the data concentrator module (DCM). The DCM organizes data and transfers them into computers for storage and later analysis. One DCM captures signal from 64 FEBs. See Fig. 2.6 for a scheme of the signal light processing [17].

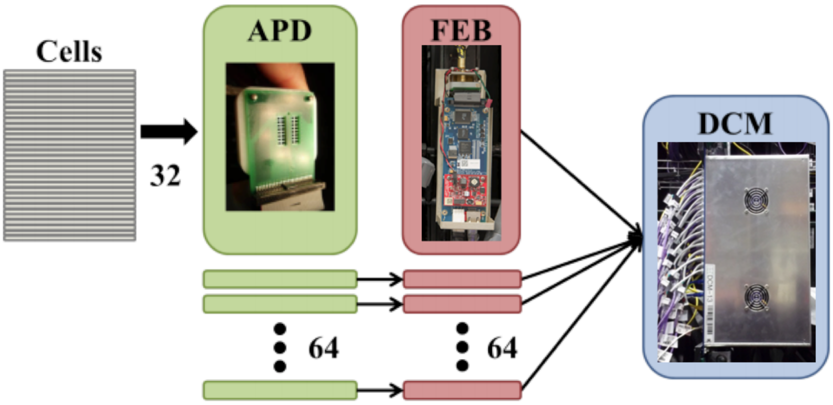

Figure 2.6: Scheme of the signal light processing. The light from 32 cells is lead to 32 pixels on one APD. The optical signal is there converted to the electronic signal. The APD is attached to a FEB where the signal is time stamped and shaped. Signal from 64 FEBs is collected by one DCM and is further transfered to computers for storage and analysis. Figure was taken from [18].

Basic cells are stacked together to form a higher structure object. A group of 16 cells make an extrusion and two extrusions (32 cells) make a module. Signal from one module is captured by one APD chip with 32 pixels. One layer of cells forms a plane which is of a different size for ND and FD. Planes in detectors are assembled in alternating horizontal and vertical positions meaning that the adjacent plane is horizontally oriented to the vertical one as can be seen in Fig. 2.7. Such layout allows for a 3-D reconstruction of the particle tracks positions. A plane number will give the z coordinate while the x coordinate comes from the vertical cells and the y coordinate from the horizontal cells. Combinations of the plane and cell number in case of vertical cells represents the x view and in case of the horizontal cells the y view. The x view can be imagined as viewing the detector from above as the vertical axis in this view represents the horizontal coordinate x and the horizontal axis shows the z coordinate. The y view can be imagined as viewing the detector from a side as the vertical axis in this case represents the vertical y coordinate in the detector and the horizontal axis again z coordinate. Correlating the x and y views provides an information about where along the cell the specific hit happened.

2.3.2 Near Detector

The ND is located 1 km downstream of the NuMI target in an 100 m underground cavern in Fermilab. It is 15.9 m long with the mass of 290 tons. The ND consists

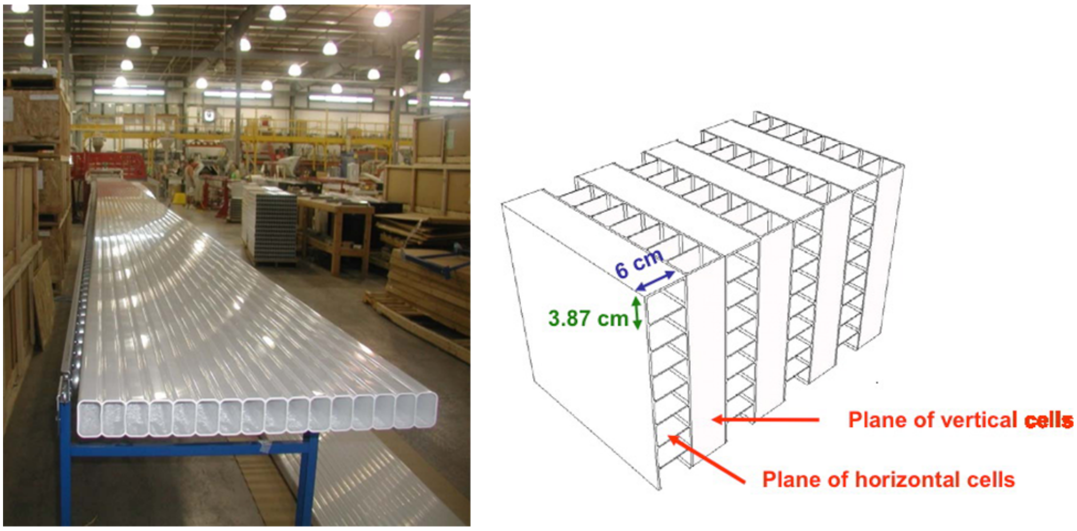

Figure 2.7: **Left**: Real life extrusion. A group of 16 cells stacked together form an extrusion. **Right**: Planes of vertically oriented cells are alternated with planes of horizontally oriented cells. Such assembly allows for a 3-D reconstruction of particle tracks positions. Figures taken from [17].

of two parts: active region and the Muon catcher. There are 192 planes in the active region, 3 modules (96 cells) per plane, each plane 4.1 m × 4.1 m. Total length of active region is 12.8 m. Muon catcher's 22 planes are 3 modules wide and 2 modules high. Active planes are interspersed with 10 cm thick steel plates in total of 10. Steel in the Muon catcher serves as a stopping element and makes sure that most of the muons from the beam interactions are fully contained in the detector.

2.3.3 Far Detector

The FD is located in Ash River, Minnesota, 810 km away from the NuMI target, at 14 mrad angle with respect to the beam center. It is 60 m long with the mass of 14 ktons. There are 896 planes in the FD, 12 modules (384 cells) per plane, each plane 15.6 m × 15.6 m. Total number of cells in the FD is 344 064. As the FD is positioned on a surface a shielding of concrete layer topped with 6 inches of high-Z loose barite rock is made on top of it to reduce the number of electromagnetic cosmic rays entering the detector unseen [17].

2.4 Reconstruction

In each cell a charge deposit or an electronic noise above a certain threshold is stored as a hit. The amount of light resulting from energy deposition recorded at the readout is represented by the ADC units. These are converted to photoelectron units (PE) as ADC/1.43 [19]. The PE units are intended to approximate the number of photoelectrons seen at the readout. Hits in individual cells are grouped together based on their space and temporal proximity in each view. Clusters of grouped hits are called slices. One slice usually represents one neutrino interaction or a single cosmic ray.

In each slice and view a simple tracking algorithm called Windowtracker is run with a result of 2-dimensional tracks. The Windowtracker takes a window of first n planes in the view and fits hits in these planes to a straight line. Resulting fit line predicts where the next hit in the following plane should be. If the hit is within a certain tolerance from the prediction Windowtracker slides the window down by one plane now fitting the former $n-1$ planes with the additional hit from the following plane. See a schema of sliding windows in Fig. 2.8. If there is no hit within a tolerance from the prediction the track is considered to end. This method accounts for possible track bending due to multiple scattering or non-linear energy loss at the end of the stopping track [20] .

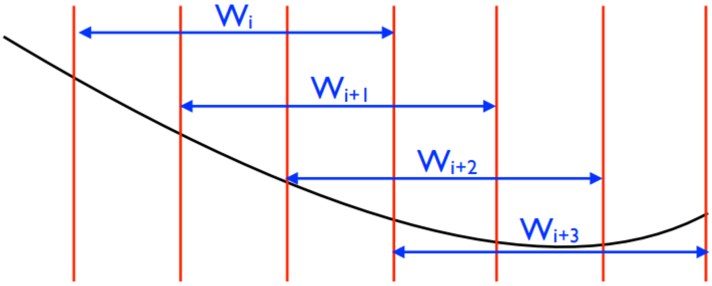

Figure 2.8: Schema of tracking algorithm Windowtracker. A window W of first n planes is taken and fit to a line. If the fit is good the window is slid by one plane down producing a window W_1 composed of $n-1$ planes from window W and one additional following plane. Figure was taken from [20].

For each slice, reconstructed 2D tracks from each view are merged to one 3D track, if the track is of good quality in each view. That is, if in each view the track crossed at least half of the planes. For further calibration, only reconstructed 3D tracks are used. Also, some additional quality criteria are applied to remove tracks that often have badly reconstructed position along the cell. The reconstructed path length of each hit in a cell has to be longer than 0.1 cm and shorter than 10 cm. A track needs to cross at least 70 cm in z direction and the value of z coordinate of unit vector of initial direction of the track has to be more than 0.2 cm to remove too steep tracks. At least 80% of hits in a slice must belong to a track. As we are using through-going muons both ends of the track should be close to the edges of the detector, therefore a reconstructed start and end of the track have to be within 10 cm to any edge of the detector. Tracks that have huge changes in the step size from one trajectory point to another are probably poorly reconstructed and are removed. Number of hit planes in each view must be consistent so that the 3D trajectory can be reconstructed properly. Therefore, the difference in plane number at a start and at an end of the track between the two views must be smaller than 3 and the asymmetry $\frac{\text{xPlanes}-\text{yPlanes}}{\text{xPlanes}+\text{yPlanes}}$, where xPlanes and yPlanes are the numbers of planes with hits in them in x view and y view respectively, must be less than 0.1.

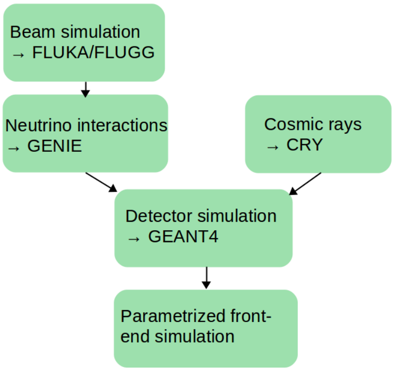

Figure 2.9: Steps in simulation chain for the NOνA experiment. See description in text. Figure taken from [21].

2.5 Monte Carlo Simulation

The simulation chain is depicted in Fig. 2.9. The first step of the simulation is modelling of the NuMI beam. That starts with producing hadrons from 120 GeV protons interacting with the graphite target as well as their decay as they travel through focusing horns and decay pipe. Simulation of the physics of particle interactions is done using FLUKA [22, 23] simulation package through the FLUGG GEANT4 [24] geometry interface, which is accounting for the environment in which particles interact. Resulting simulated beam of neutrinos is stored in flux files with the information of their flavour, energy, momentum and parentage. Flux files are then input to neutrino event generator GENIE [25] which determines whether a neutrino has interacted with the detector and simulates the resulting particles of such interaction together with their kinematic properties. Along with the beam the cosmic rays are simulated. The simulation package CRY [26] generates the flux list of particles created in cosmic ray showers. In the next step particles created in neutrino interactions and in cosmic showers are propagated through the detector using GEANT4 [27, 28] producing simulated energy deposits in the active material.

High flux of neutrinos near the ND results in not only several interactions per spill in the detector but also in many interactions in the rock surrounding it. These events are called “rock events” and muons coming from these interactions are called “rock muons”. To simulate these events, GEANT4 is allowed to propagate muons through a large amount of rock and those that will make it to and leave some energy in the detector are stored.

In the final step the list of energy deposits is passed to a parametrized front-end simulation. This step involves converting simulated energy deposition into photons, capturing and propagating them through the fiber to the APD and simulating the readout response. The final output is in the format of raw data same as the output of the actual real life detector [8, 21].

3. Calibration of the NOνA detectors

The goal of the calibration of the NOνA detectors is to convert the detected raw signal into physically meaningful units representing the energy a particle deposited in a cell. The process includes smoothing inequalities in a detector response to a given deposited energy in-cell and between cells that may arise from different factors as well as assigning the correct energy scale to a given response. Muons are used as a standard candle for the calibration because their energy deposition is nearly uniform along their trajectory and is relatively flat for energies between 1 and 100 GeV. The NOνA experiment is currently using cosmic muons for the calibration of both detectors. In this thesis, calibration of the ND using simulated rock muons is studied and compared to the standard cosmic calibration.

3.1 Calibration

The calibration workflow consists of two main parts: relative and absolute calibration. The relative calibration corrects a detector response to a given energy deposition to be uniform across the detector. It consists of drift, threshold, shadowing and attenuation correction. The drift correction should erase the variations in response over time due to, *e.g.*, seasonal temperature or scintillator degradation but has not yet been implemented. The threshold, shadowing and attenuation corrections are described in more detail in Sections 3.2.1, 3.2.2, 3.2.3, respectively. The absolute calibration finds the proper factor by which a multiplication of output units from the relative calibration will result in the recorded energy in physically universal units such as GeV. In this thesis the relative calibration to correct for the shadowing, threshold and attenuation effects is presented.

3.2 Relative calibration

In this and next sections the main focus will be on the following variables:

- R[PE]: A raw detector response. It's value is an approximation of number of photoelectrons (PE) recorded at the readout.
- R^{n}[PE/cm]: A normalized detector response per path length unit calculated as R divided by path length in a cell.
- R_{corr}[PE$_{\mathrm{corr}}$]: A corrected detector response.
- $R^{\mathrm{n}}_{\mathrm{corr}}$[PE$_{\mathrm{corr}}$/cm]: A corrected normalized detector response.

The attenuation calibration corrects for the attenuation of light when the light travels through the optical fiber in the NOνA cell. It is done by performing fits on plots of the normalized detector response R^{n} vs coordinate W representing the position along the cell where $W = 0$ at its center. However, there are several effects, namely the threshold and shadowing effects, that vary the distribution of R^{n} vs W which thus shift the mean of the R^{n} value. For the attenuation calibration the mean value of R^{n} is used, so before proceeding to it the threshold and shadowing effects have to be already corrected. The corrections for these effects are derived from a simulation.

3.2.1 Threshold correction

There is a threshold for a value of the recorded PE to be accepted as a hit. However, the number of photoelectrons produced at the readout follows a Poisson distribution. Therefore it can happen that a hit that shouldn't pass the threshold generates a higher number of photons and mimics a behaviour of a higher PE hit. This can result in overestimation of a light-level and subsequently bias the real hit energies to lower values after the attenuation correction. In order to obtain the best estimate of the total energy deposited in scintillator this effect has to be corrected for.

Since the light attenuates while travelling through the fiber, the threshold effect is dependent on the coordinate W. The threshold correction is calculated as:

$$\mathrm{Corr}_{\mathrm{thresh}}(W) = \mathrm{Mean}(R_{\mathrm{mip}}/\lambda_{\mathrm{Poisson}}), \tag{3.1}$$

where R_{mip} is a simulated response of minimum ionizing particle (MIP) used for the calibration and $\lambda_{\mathrm{Poisson}}$ is the number of simulated photons which would be seen at the readout in the absence of fluctuations. The correction is applied as:

$$R^{\mathrm{thresh}}_{\mathrm{corr}} = R/\mathrm{Corr}_{\mathrm{thresh}}(W). \tag{3.2}$$

See Fig. 3.1 for example of the threshold correction for the simulated rock muons in the ND. Shown are the values calculated as a mean through all cells in the active region of the ND.

3.2.2 Shadowing correction

The attenuation calibration is designed in a way that muons used for the calibration are expected to deposit constant amount of energy along their whole path and that the energy of all these muons is comparable as well as their energy deposition rate. However, this assumption is not generally fulfilled. To calibrate the whole detector we also need to account for higher energetic muons that reach distant parts of the detector: a bottom of the detector in case of the cosmic muons and the back of the detector in case of the rock muons. These higher energetic muons may have a different deposition rate than those less energetic. This effect is known as shadowing as size of the detector prevents the less energetic muons to reach the end of the detector. To even out the deposition rate of muons through the whole used energy range and fulfill the attenuation calibration condition the shadowing effect needs to be corrected for. This effect is much more significant in the bigger FD but to keep the calibration workflow same for both detectors correction is made for the ND cells, also.

The shadowing correction flattens the energy deposition rate of particles used for calibration to the constant MIP value throughout the whole detector. The

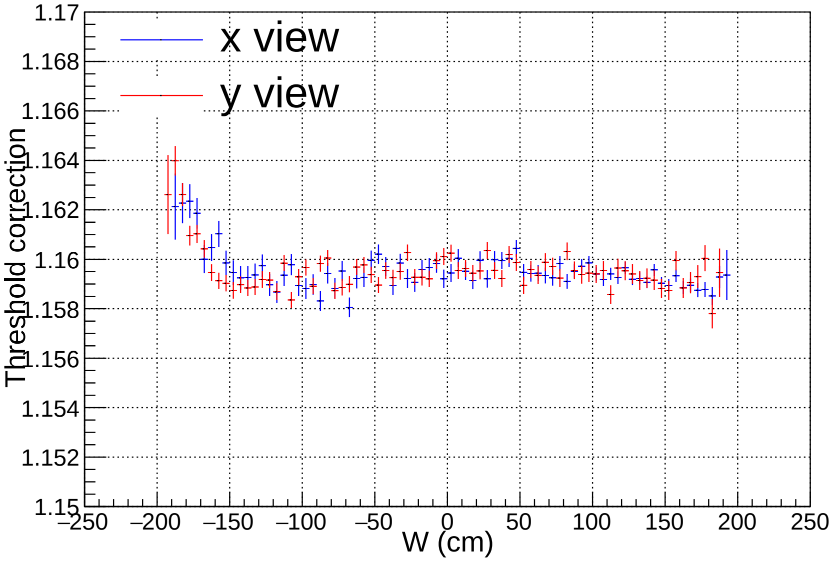

Figure 3.1: Mean threshold correction for simulated rock muons in the active region of the ND. Comparison between x view (blue points) and y view (red points).

shadowing correction is calculated as:

$$\mathrm{Corr}_{\mathrm{shadow}}(W) = \mathrm{Mean}\left(\frac{E_{\mathrm{true}}}{E_{\mathrm{mip}}}\right) = \mathrm{Mean}\left(\frac{E_{\mathrm{true}}}{\mathrm{Path}_{\mathrm{reco}} \times 1.78\ \mathrm{MeV/cm}}\right), \tag{3.3}$$

where E_{true} is the true energy of a given hit known from the simulation truth information and E_{mip} is the predicted energy the MIP particle deposited in a cell calculated as reconstructed path length $\mathrm{Path}_{\mathrm{reco}}$[cm] multiplied by 1.78 MeV/cm which is dE/dx of MIP in the scintillator. The correction is applied as:

$$R^{\mathrm{shadow}}_{\mathrm{corr}} = R/\mathrm{Corr}_{\mathrm{shadow}}(W). \tag{3.4}$$

See Fig. 3.2 for example of shadowing correction for the simulated rock muons in the ND. Shown are the values calculated as a mean through all cells in the active region of the ND.

3.2.3 Attenuation correction

The purpose of the attenuation calibration is to provide constants such that an amount of energy deposited in the detector and registered by an APD can be expressed in comparable units, $\mathrm{PE}_{\mathrm{corr}}$, no matter where the deposition occured. An energy deposit R_{corr} expressed in $\mathrm{PE}_{\mathrm{corr}}$ is independent of the distance from the APD which read out the signal.

The attenuation calibration is performed in the following way. First, we take a sample of through-going muons. Next, we create a 2D histogram of R^{n} vs W for each studied view x and y. In the ND the values of W are in the range $[-200, +200]$ cm with an exception of the Muon catcher vertical cells which have the values of W within the range $[-200, +100]$ cm. Next, we construct a 1D

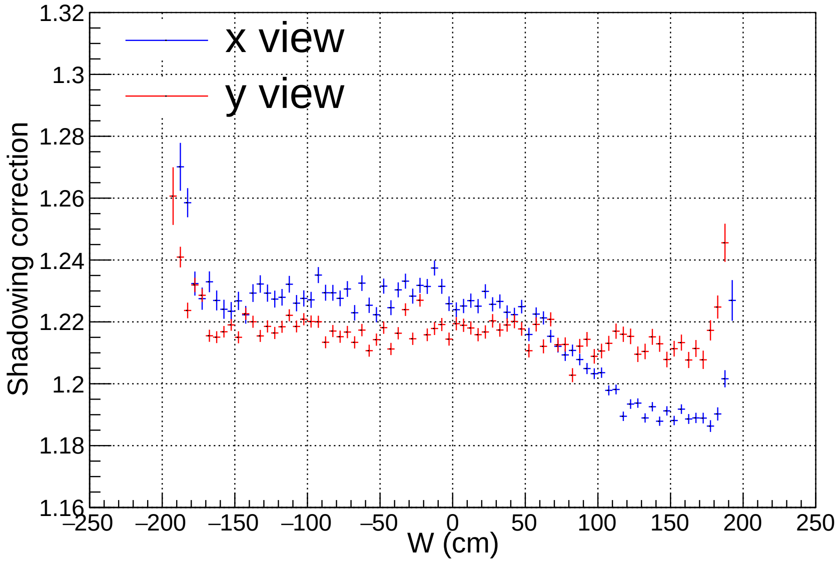

Figure 3.2: Mean shadowing correction for simulated rock muons in the active region of the ND. Comparison between x view (blue points) and y view (red points).

histogram from the 2D histogram by taking the median value of R^{n} in each W bin. Additionally, we apply a combined threshold and shadowing correction factor T as

$$R_{\mathrm{corr}} = \frac{R}{T}, \tag{3.5}$$

where T factor is calculated from Eqs. (3.1) and (3.3) as

$$T = \frac{R_{\mathrm{mip}}}{\lambda_{\mathrm{Poisson}}} \frac{E_{\mathrm{true}}}{E_{\mathrm{mip}}}. \tag{3.6}$$

Finally, the resulting 1D histograms — with applied threshold and shadowing correction — are a subject to the attenuation fit, so the variable R^{n} is substituted by $R^{\mathrm{n}}_{\mathrm{corr}}$. See Fig. 3.3 for example of the uncorrected R^{n} values of the simulated rock muons in the ND. We show the values calculated as a mean through the whole active region of the ND. To see the effect of the application of the threshold and shadowing corrections to the histograms in Fig. 3.3 see histograms in Fig. 3.4.

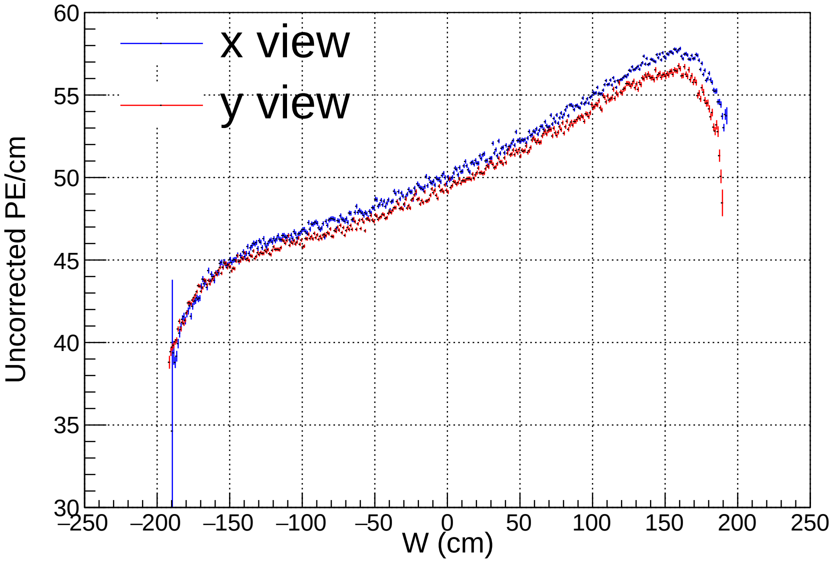

Figure 3.3: Simulated mean R^{n} before any correction in the active region of the ND. Comparison between x view (blue points) and y view (red points).

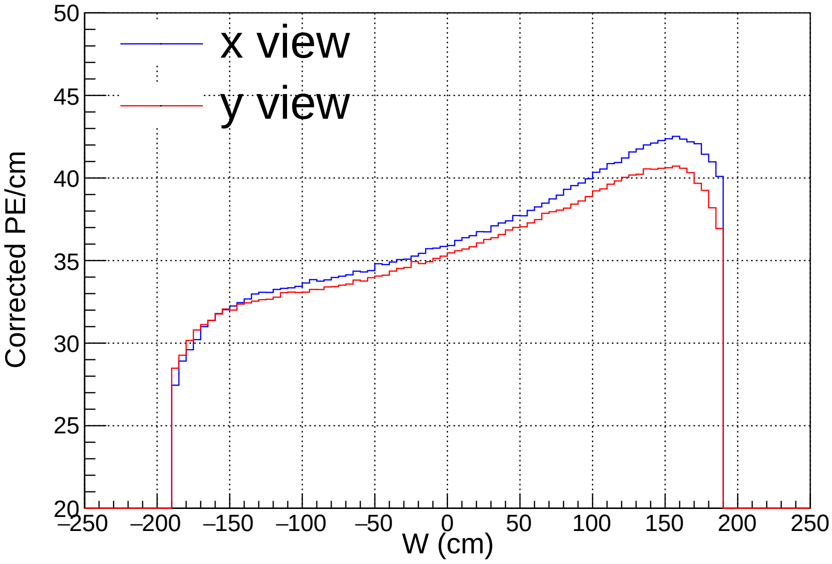

Figure 3.4: Simulated R^{n} after applied treshold and shadowing corrections, called $R^{\mathrm{n}}_{\mathrm{corr}}$, in the active region of the ND. Comparison between x view (blue curve) and y view (red curve).

The final stage of the attenuation calibration is fitting the response $R^{\mathrm{n}}_{\mathrm{corr}}$ (on y-axis) vs W (on x-axis) to the double exponential function which has a form:

$$y = C + A\left(\exp\left(\frac{x}{X}\right) + \exp\left(-\frac{L+x}{X}\right)\right), \tag{3.7}$$

where L is the cell length, C, A and X are the free parameters in the fit. Parameter C is typically called the background, parameter X the attenuation length and parameter A is an overall scaling factor for the attenutation correction. This function accounts for the light travelling by the shortest path through the fiber $\left(\exp\left(\frac{x}{X}\right)\right)$ as well as for the longer path around $\left(\exp\left(-\frac{L+x}{X}\right)\right)$. To evaluate the quality of the fit we calculate the square of the mean fractional deviation of the data from the fit, χ^2, for each cell and each fit. If a value of χ^2 exceeds 0.2 the channel is marked as uncalibrated.

The simulation we use doesn't account for any differences among cells. However, in the real detector there can be slight variations, for example in fiber position in the cell. Therefore it is needed to calculate the attenuation correction for each cell individually [16, 29].

4. Rock muon sample selection

Since we are using only simulated data in this thesis which contain all the information about the particle's origin it could be very easy to select a pure sample of any preferred particles. However, the purpose of this study is to examine useful methods for the calibration of the real detector. Therefore we need to make sure the methods are extendable to be used with the real data as well. With that in mind we developed the selection criteria on reconstructed variables available for the simulated data as well as for the experimental data. The goal was to select tracks belonging to rock muons out of all the tracks seen by the detector with a reasonable confidence.

The development of the selection criteria is done using simulation where it is possible to evaluate their accuracy based on the truth information. Conditions on what track is considered to belong to a rock muon were defined as follows:

- PDG code of the particle the track belongs to must be 13. That number stands for muons according to [4].
- PDG code of the mother particle of the particle the track belongs to must be 14. That number stands for muon neutrinos according to [4].
- The interaction by which the particle the track belongs to was created must be the charged-current interaction.
- The interaction by which the particle the track belongs to was created must have the true vertex anywhere outside the detector.

Tracks that fulfill these conditions are further marked as 'rock' events. The goal was to have significant predominance of these tracks in the selected sample while keeping the number of tracks that don't fulfill these conditions low. Tracks that don't satisfy any of these requirements are further marked as 'detector' events even though also non-detector events, like neutral-current rock events, would belong to this group. Rock events are considered as the signal and detector events as the background.

The quality of the chosen selection criteria is evaluated based on variables efficiency (ϵ) and purity (p). The efficiency reflects how many of all the true rock muon tracks present in the examined dataset were correctly captured by the selection criteria. It is calculated as:

$$\epsilon = \frac{\text{number of true rock muon tracks selected}}{\text{number of all true rock muon tracks}}. \tag{4.1}$$

The purity reflects how many selected tracks are correctly selected true rock muon tracks. Purity is calculated as:

$$p = \frac{\text{number of true rock muon tracks selected}}{\text{number of all selected tracks}}. \tag{4.2}$$

The higher the value of both of these variables the better. The goal is to maximize them as much as possible.

4.1 Dataset

For the development of the selection criteria a NuMI beam simulation file with 2000 events was used. One event in this file contains all activity in the detector during 500 μs window centered around one beam spill lasting for 10 μs [16]. Since the flux of neutrinos in the ND is high several neutrino interactions per one spill and per one event can occur. Therefore in one event also several reconstructed tracks can be found. This file lacks any cosmic activity. In the ND the rate of cosmic rays is about 1 Hz and since the recorded window is only 500 μs long the cosmic activity in the beam simulation files would be negligible.

4.2 Selection variables

We have studied distributions of several reconstructed variables which would presumably reflect the differences between rock and detector events. Among these, three variables have shown themselves to be reasonable and also sufficient to make constraints. The first one is a reconstructed start position of the track (start_x, start_y and start_z for the x, y and z coordinate respectively). The second one is a cosine of the angle between the track and the direction of the beam axis ($\cos\theta$). The last one is a variable which evaluates how many cells in a slice with recorded hits are part of the track (f_{slice}). It can be expressed in a simple form as

$$f_{\text{slice}} = \frac{\text{number of cells on a track}}{\text{number of hit cells in a slice}}. \tag{4.3}$$

The motivation behind choosing these variables is discussed in following sections.

4.2.1 Selection by the reconstructed start position of the track

The start position of the track is a good variable for distinguishing between rock events and detector originated events. The rock events take place outside of the detector so tracks of particles from the rock events would enter the detector from outside through the front face or the sides and have their reconstructed start positions in the first few planes from the edges of the detector. On the contrary events which took place in the detector would have their reconstructed start position inside of the volume of the detector. We see a confirmation of this in plots of start_z in Fig. 4.1 and on plots of start_x vs start_z, start_y vs start_z and start_x vs start_y in Fig. 4.2. The rock events have peaks at the relevant edges of the detector while the detector events tend to have a uniform distribution.

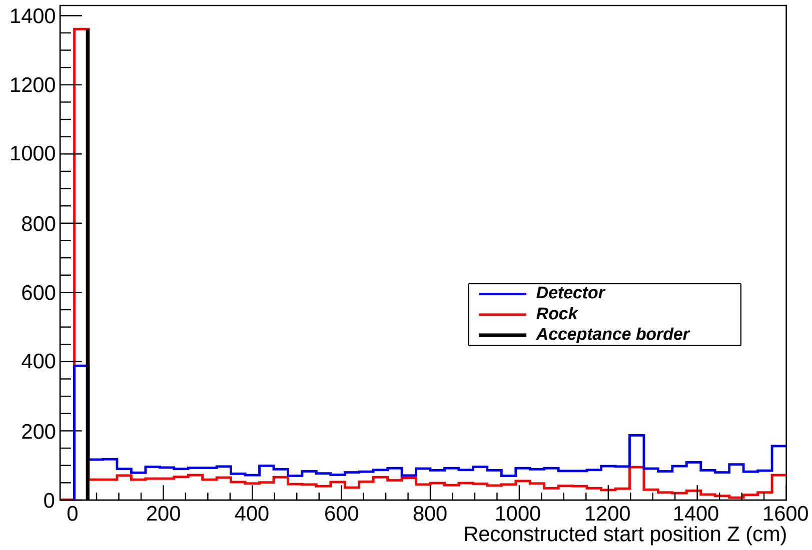

Figure 4.1: Distributions of the start$_z$ for rock (red) and detector (blue) events. In the first 30 cm the rock events are prevailing. This is caused by rock muon tracks coming through the front face of the detector. The smaller blue detector peak at the first 30 cm is caused by the tracks coming from outside but not being rock muons. The black line at 30 cm suggests a border acceptance value. Only tracks with start$_z$ smaller than this value will be taken into the selection.

4.2.2 Selection by the angle cos θ

The muons usually don't change much their direction until the very end of their tracks. The cos θ of the tracks of the particles from the rock events, especially muons, is close to 1, *i.e.* their direction is very close to the direction of the beam. That is because these muons originate from the neutrinos of the beam. The ν_μ can also interact with the nuclei in the detector by so called deep inelastic scattering. The result of such interaction is generally large number of hadrons scattering to wide variety of angles. Therefore, by setting a condition of selecting tracks with their direction close to the direction of the beam we filter these hadrons out. In the histograms of cos θ distributions in Fig. 4.3 we can see a significant skew of the values towards 1 for rock events over detector events.

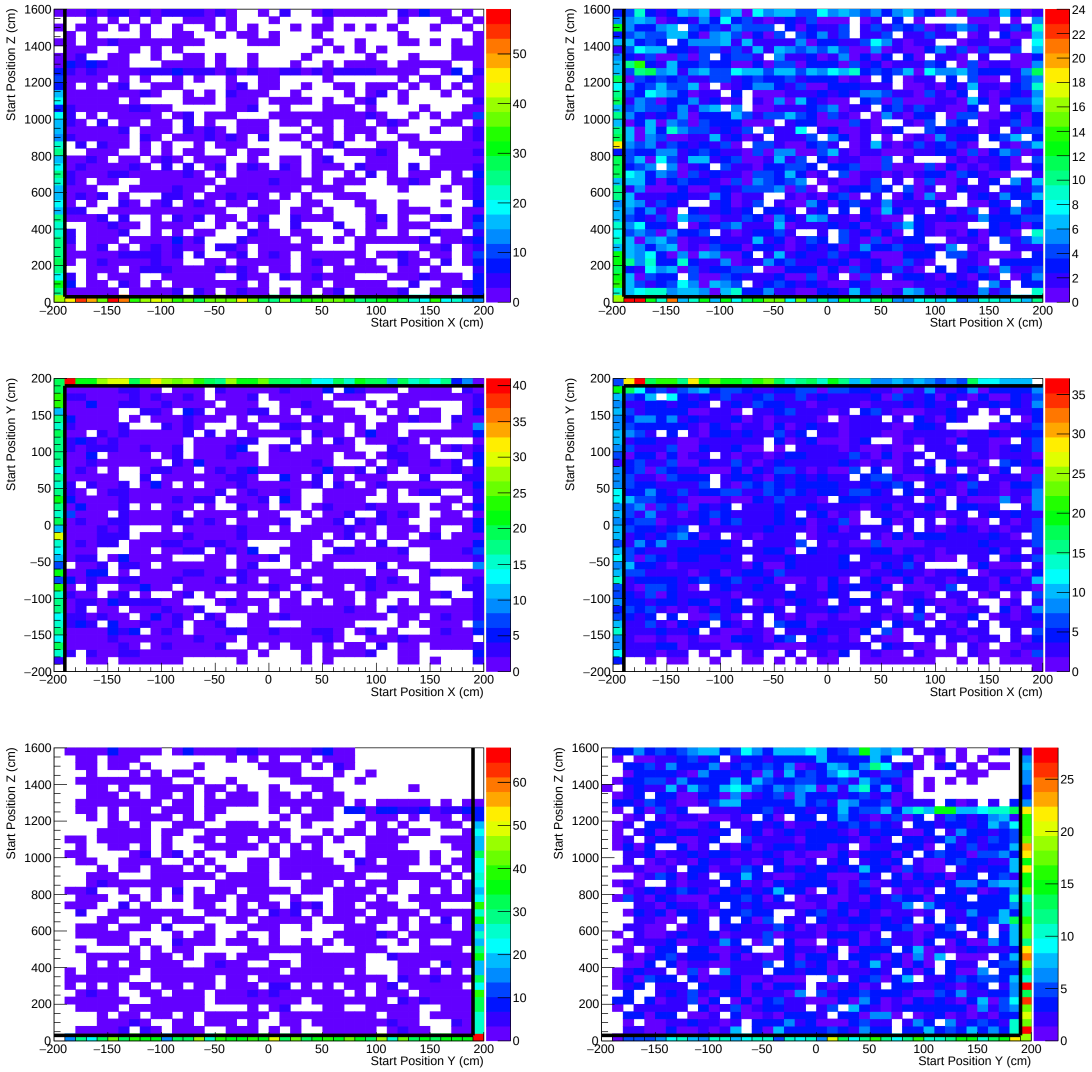

Figure 4.2: These plots show the different 2D distributions of individual reconstructed start position coordinates. **Left**: Rock events. **Right**: Detector events. The detector distributions are quite uniform across the whole detector. Contrary to that the rock distributions manifest the track starts at the edges of the detector. Most rock events with start$_z$ $>$ 30 cm start within 10 cm of the left side edge of the detector when looking along the direction of the beam (see left-top plot) and within 10 cm of the top side of the detector (see left-bottom plot). The black lines represent the acceptance borders for the selection.

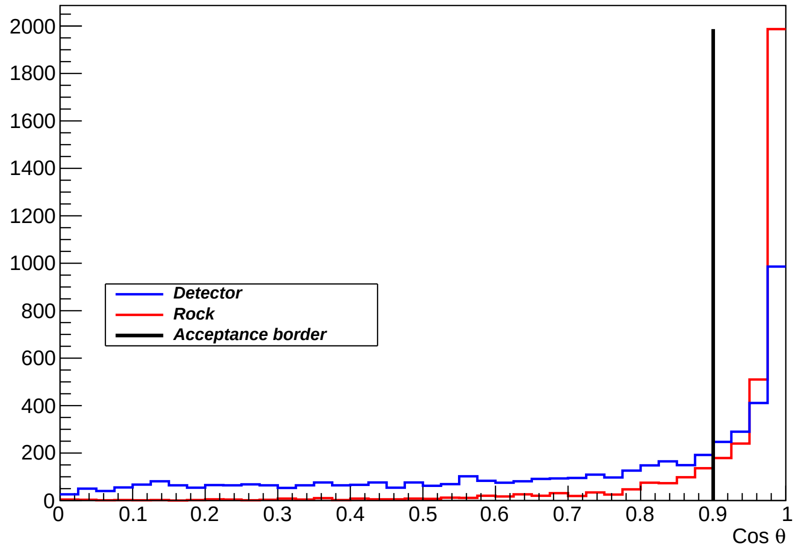

Figure 4.3: Distribution of the cos θ for rock (red) and detector (blue) events. Altough all the tracks originating from the beam tend to have the direction more or less close to the direction of the beam the cos θ at the value around 1 is more populated by the rock events.

4.2.3 Fraction of the number of cells on a track and in a slice (f_{slice})

The f_{slice} variable is very efficient in distinguishing muons from other particles, especially those that create electromagnetic showers like electrons. The electromagnetic shower spreads through many cells in every single plane while muon's track usually hits only one cell per plane. As the track reconstruction algorithm Windowtracker assigns to a track only hits closest to the fit, it would neglect most of the other hits in each plane in the case of electromagnetic shower. Therefore the fraction of number of hit cells on the track and number of hit cells in the whole slice would be close to 0. On the other hand, reconstructed muon track would have the value of this fraction close to 1. The described difference is very well visible in a plot of f_{slice} rock and detector events distributions in Fig. 4.4.

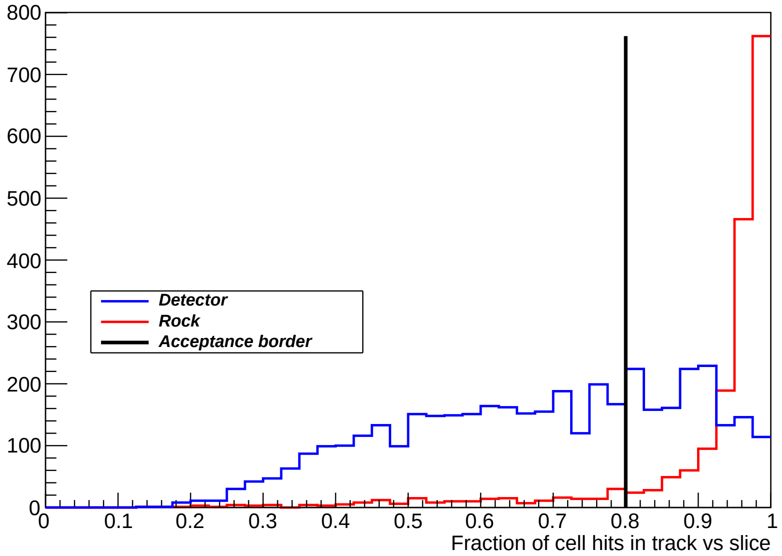

Figure 4.4: Distribution of the f_{slice} for rock (red) and detector (blue) events. The detector distribution is broad while the rock distribution peaks at 1 as expected.

4.3 Performance of the Selection 1

In this section a performance of the Selection 1 is presented. In Section 4.3.1 the specific selection criteria are introduced. In Section 4.3.2 the $N-1$ plots of chosen variables are shown. The $N-1$ plot of certain variable is a distribution of a variable after all criteria except the criterion on the plotted variable were applied. They expose how the distributions of variables change after applying the other criteria. It was helpful to examine these plots to additionaly optimize the selection criteria.

In Section 4.3.3 the overall performance of the Selection 1 is presented together with the cells vs planes plots. A cells vs planes plot is a 2D histogram of plane numbers on horizontal axis and cell numbers on vertical axis. Each bin represents one cell and value in each bin represents the number of the selected tracks that hit that particular cell. A cells vs planes plot expresses the coverage of the selected tracks in the detector. The cells vs planes plots presented are made with the full set of 1000 files further used for the actual calibration. Therefore they represent the actual coverage of the selected sample.

4.3.1 Selection 1 criteria

The selection criteria for the Selection 1 were chosen as follows:

- **start position:**
  - $\text{start}_z < 30$ cm OR
  - $\text{start}_z > 30$ cm AND $\text{start}_x < -190$ cm AND $\text{start}_y > 190$ cm
- **cos θ:**

  - *cos* $\theta > 0.9$

- $\boldsymbol{f_{\text{slice}}}$**:**
  - $f_{\text{slice}} > 0.8$

4.3.2 $N-1$ plots

In Fig. 4.5 is a plot of start$_z$ after applying the f_{slice} and cos θ criteria.When compared to the plot before any adjustments in Fig. 4.1 the detector events got considerably lower through the whole range. Similar result can be seen in the plots of other reconstructed start coordinates in Fig. 4.6. In Fig. 4.7 is the plot of cos θ after applying start and f_{slice} criteria. The detector events are well shifted to the values very close to 1 compared to the before plot in Fig. 4.3 where the detector events distribution is much wider and in most of the range prevalent over the rock events. In Fig. 4.8 is a plot of f_{slice} after applying start and cos θ criteria. In this case the effect of these modifications is the most significant compared to the before plot in Fig. 4.4. Mentioned figures show that the goal to create a sample of prevailing rock muons was reached.

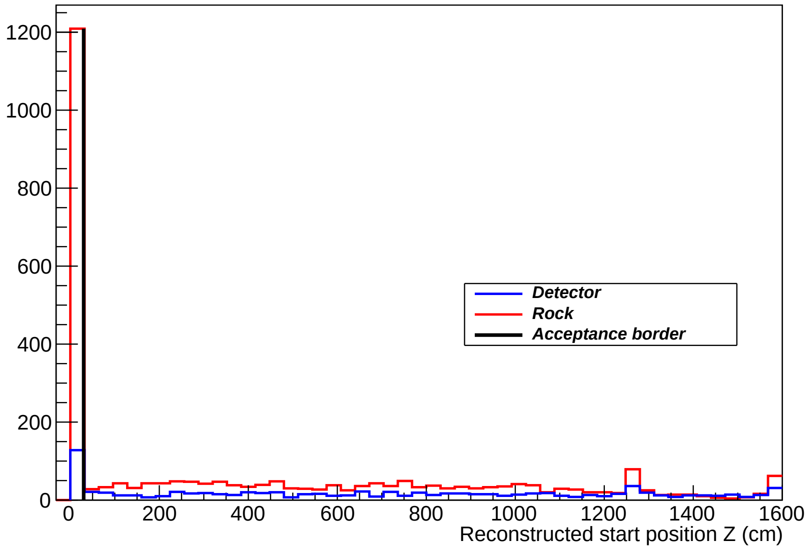

Figure 4.5: The Selection 1 $N-1$ plot of start position z coordinate. The detector events are below the rock events throughout the whole range.

4.3.3 Selection 1 Summary

In the Table 4.1 the stats of the Selection 1 are shown. With the 1226 rock tracks that passed the criteria out of all the 3645 rock tracks in the test file and with the total of 1352 tracks passing the criteria the efficiency and purity values are:

$$\epsilon = 33.6\% \quad (4.4)$$

$$p = 90.6\% \quad (4.5)$$

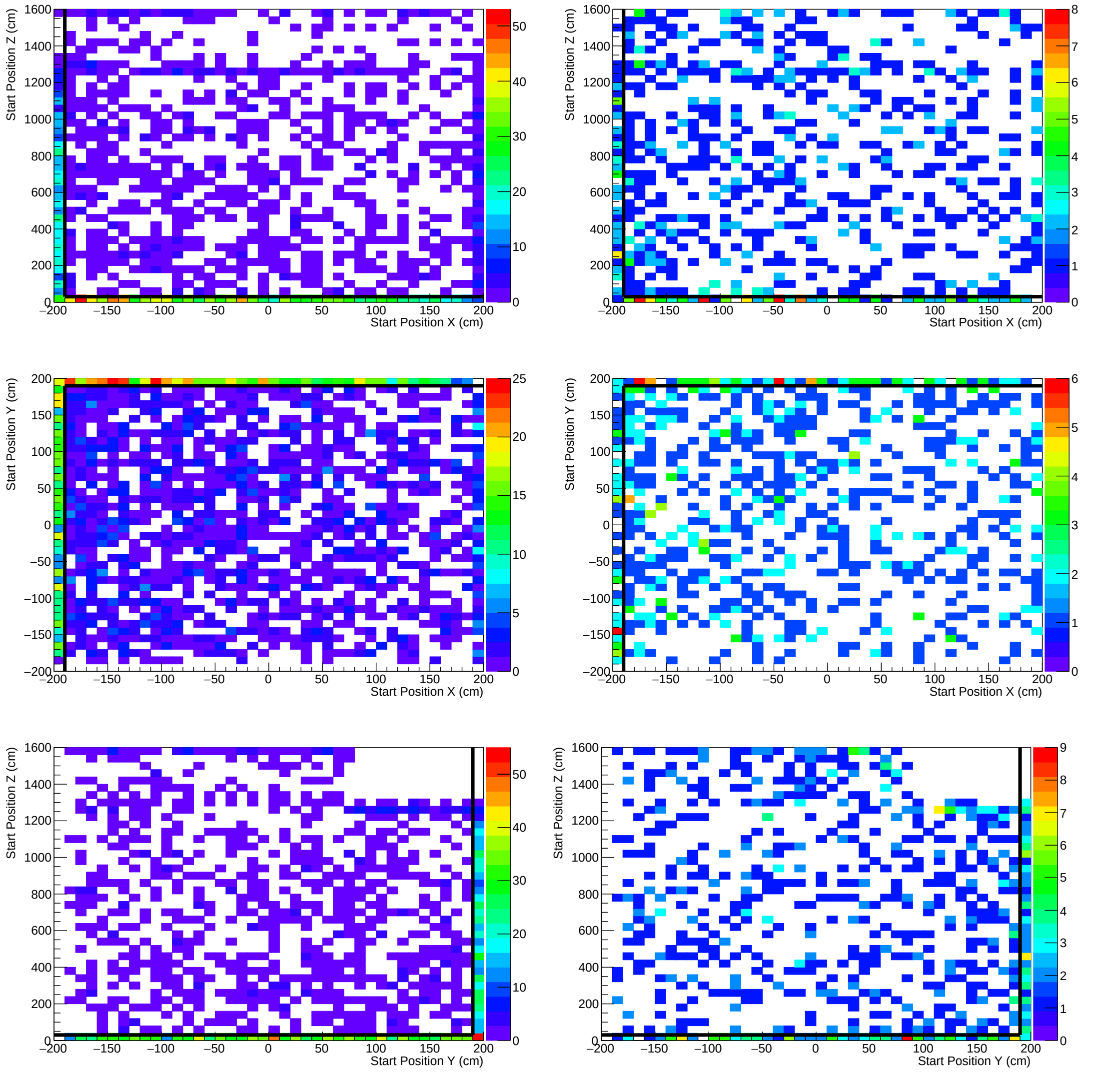

Figure 4.6: The Selection 1 $N-1$ 2D plots of reconstructed start position coordinates. **Left**: Rock events. **Right**: Detector events. The rock events preserved the distributions while the detector events lowered their numbers rapidly after applying the selection criteria when compared to the before plots in Fig. 4.2

.

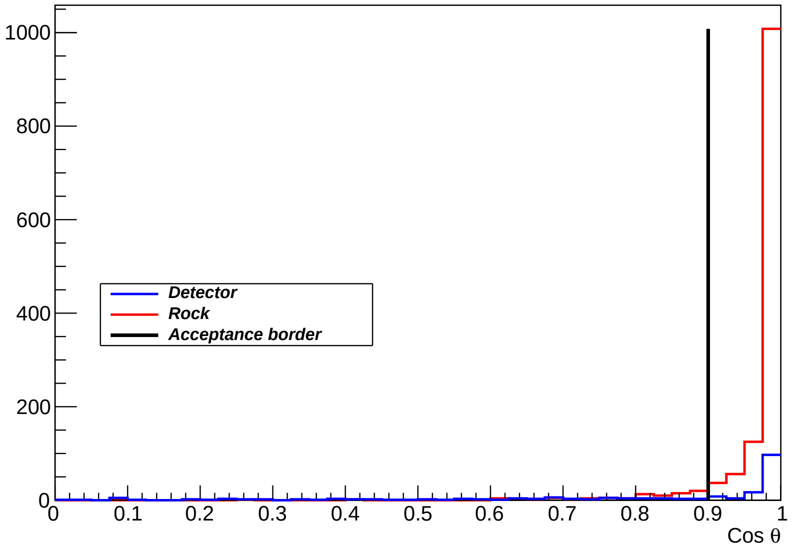

Figure 4.7: The Selection 1 $N-1$ plot of cos θ.

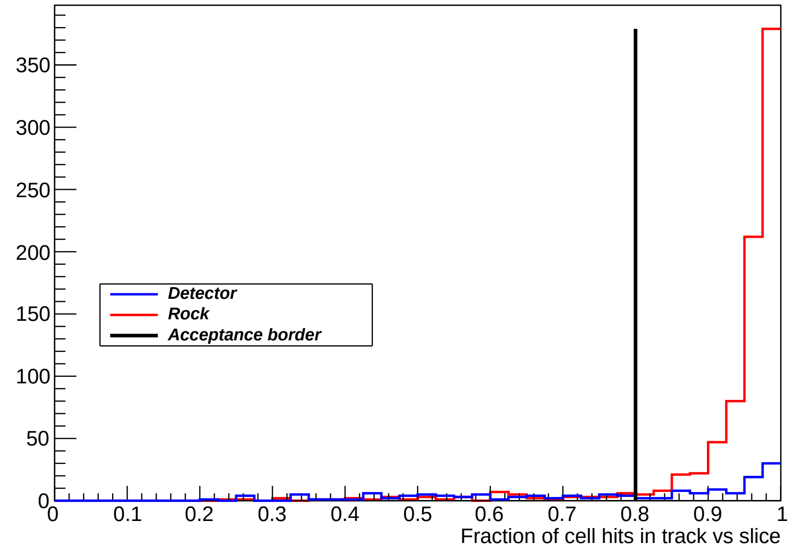

Figure 4.8: The Selection 1 $N-1$ plot of f_{slice}.

To demonstrate the overall effect of the Selection 1 criteria the plot of the track lengths after all criteria applied is shown in Fig. 4.9. The prevailance of the rock events is apparent.

The coverage of the ND by the Selection 1 tracks is shown in cells vs planes plots Fig. 4.10, x view left and y view right. The missing values at around plane 60 in x view and plane 10 in y view are the masked channels. Some issue with these channels was discovered in the real ND, such as switched cables, and it is known that data from these channels would be incorrect. Even that this is the MC data, since everything is compared to real data masking is done also on MC to preserve consistency. The coverage is good at the front and middle part of the detector but values around 2000 in the back part of the detector predict possible issues for calibration due to low statistics.

Table 4.1: Selection 1 stats.

Total number of tracks in file	8543
Total number of rock muon tracks in file	3645
Number of Rock tracks that passed the cuts	1226
Number of Detector tracks that passed the cuts	126

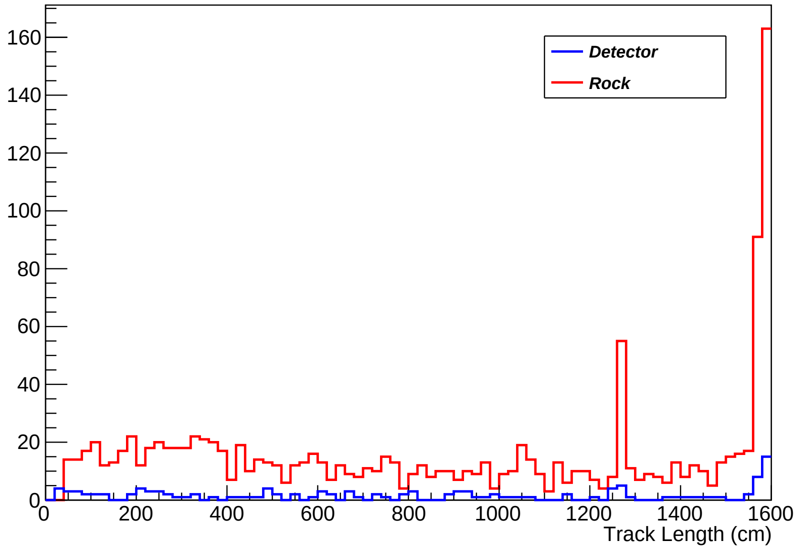

Figure 4.9: The distribution of the track lengths after applying all the Selection 1 criteria for the rock (red) and detector (blue) events. The prevailance of the rock events is a good proof of the selection effectiveness. The peak around 1300 cm is caused by the tracks stopping in the first planes of the Muon catcher. The peak at 1600 cm marks the end of the detector as it's caused either by the tracks stopping in the end planes of the detector and by the throughgoing tracks.

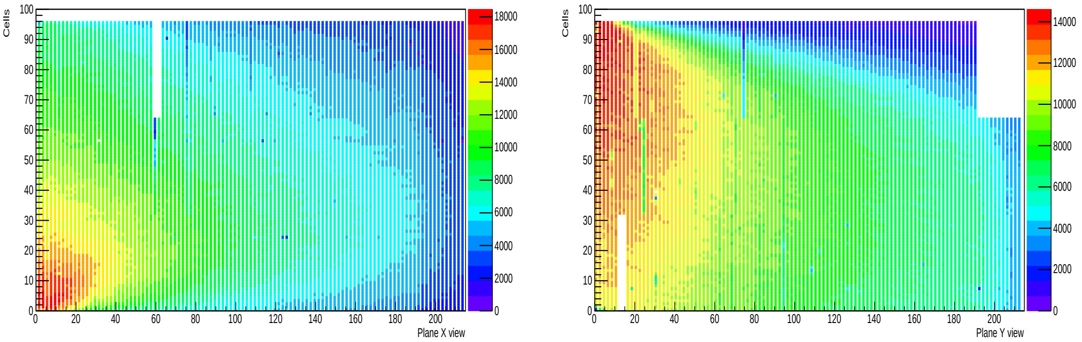

Figure 4.10: The cells vs planes plots representing the coverage of the ND by the Selection 1 sample tracks. **Left**: x view. **Right**: y view. The holes in the plots are the masked channels. The blank space in the y view right top corner is due to shorter vertical dimension of the Muon catcher.

4.4 Misreconstructed end position issue

One of the studied variables, reconstructed end position of the track, showed suspicious behaviour. Its z coordinate (end_z) would have a peak at values less than 30 cm, see Fig. 4.11, similar to a peak at the same value in start_z plot, see Fig. 4.1. That similarity lead to a hypothesis that in some cases the tracking algorithm Windowtracker somehow switched the start and end position of the track. The hypothesis was confirmed by looking at the event displays of the tracks with $\text{end}_z < 30$ cm. The event display is a graphical representation of collected

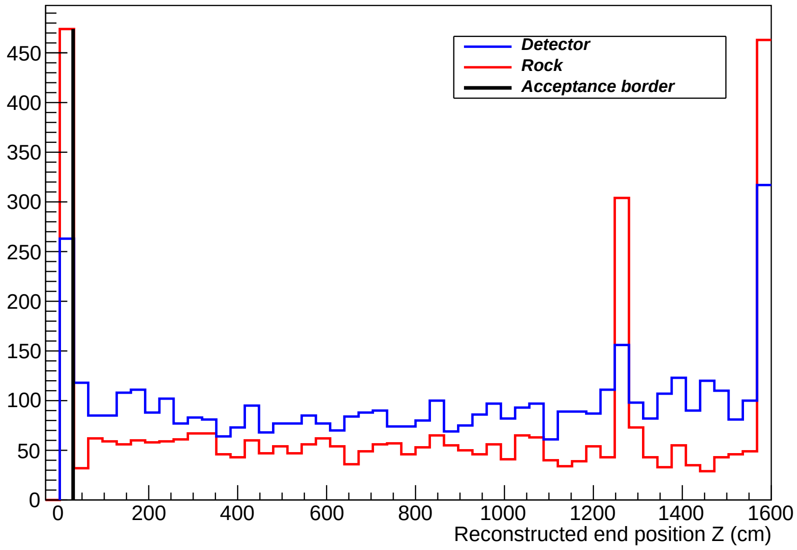

Figure 4.11: Distribution of the end_z variable, comparison between rock and detector events. Notice the peaks at 30 cm. Tracks with the values less than 30 cm could belong to rock particles ending in the first planes of the detector, however, there's no natural reason for them to be so numerous.

hit information overlayed on a schematic of the detector. It typically shows x and y view. An example of the event display of the track with $\text{end}_z < 30$ cm is shown in Fig. 4.12. The common property of all the studied suspicious tracks

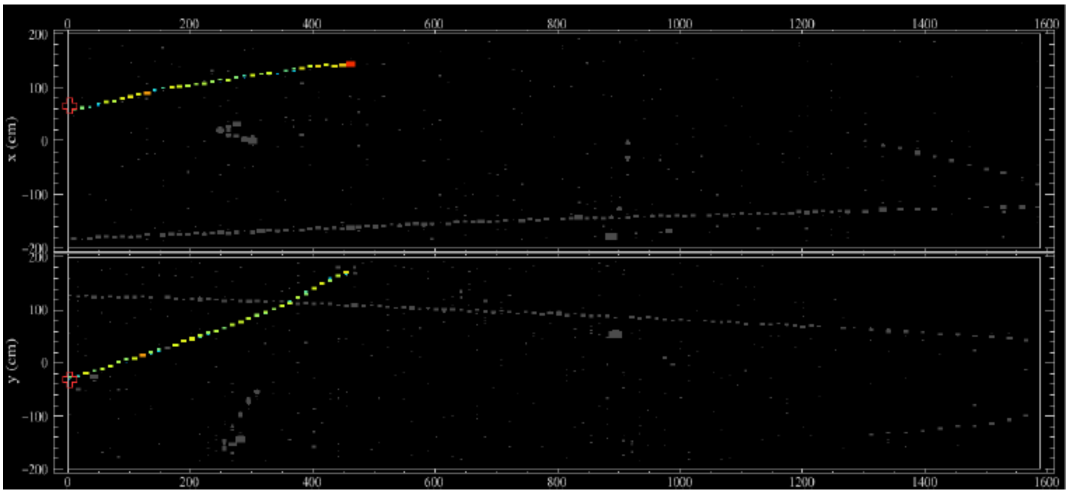

Figure 4.12: Event display of the track with misreconstructed start and end position. **Top:** x view. **Bottom:** y view. From the y view we can see that the track is upgoing. However, the reconstructed start position was assigned to the upper point and end position to the lower point which is obviously incorrect.

was their direction. They all were upgoing with the beginning of the track being marked as the end and vice versa. The tracks with the $\text{end}_z > 30$ cm were all downgoing with correctly assigned start and end position coordinates. The reason behind this misreconstruction showed up to be in one characteristic of the tracking algorithm. Since it was primarily developed to quickly and effectively reconstruct the cosmic muon tracks which are coming from above the Windowtracker would automatically assign the end of the track with higher y coordinate value as a start position and the end with lower y coordinate value as the end position. That is correct for the cosmic muons, however, for the rock muons with upward direction the Windowtracker would switch the start and end position of the track and that would cause the suspicious peak in the end_z plot.

Since one of the selection criteria is to take only tracks with the reconstructed start position close to the edges of the detector all the upgoing tracks would be lost. By losing all the upgoing tracks not only the efficiency would decrease but it would also lower the chance that the cells in the corners of the detector where downgoing tracks can hardly reach, upper far corners and bottom near corners, would get calibrated. Therefore, a separate set of selection criteria needed to be developed to include also upgoing tracks. It was done on the same variables but instead of the reconstructed start position the reconstructed end position was constrained.

The final set of the selection criteria would consist of the former Selection 1 merged with the edited ones accounting for the tracks with misreconstructed start and end position further referred to as Selection 2. So the final sample of the selected tracks would consist of tracks that would pass either of the selection criteria sets.

4.5 Performance of the Selection 2

In this section the Selection 2 specifically adjusted to recover the tracks with misreconstructed start and end position is presented. In Section 4.5.1 the selection criteria are summarized. The $N-1$ plots with Selection 2 criteria applied are discussed in Section 4.5.2. In Section 4.5.3 the properties of the Selection 2 are presented along with the efficiency and purity values and the cells vs planes plots.

4.5.1 Selection 2 criteria

The selection criteria for the Selection 2 were chosen as follows:

- **start position:**
  - $\text{end}_z < 30$ cm
- **cos θ:**
  - $\cos\theta > 0.82$
- **f_{slice}:**
  - $f_{\text{slice}} > 0.92$

4.5.2 $N-1$ plots

In Fig. 4.13 is a plot of end_z after applying the f_{slice} and $\cos\theta$ criteria. In Fig. 4.7 is the plot of $\cos\theta$ after applying end_z and f_{slice} criteria. In Fig. 4.8 is a plot of f_{slice} after applying end_z and $\cos\theta$ criteria. When compared to the plots before any adjustments in Fig. 4.11,Fig. 4.3 and Fig. 4.4, the detector events got considerably lower through the whole ranges.

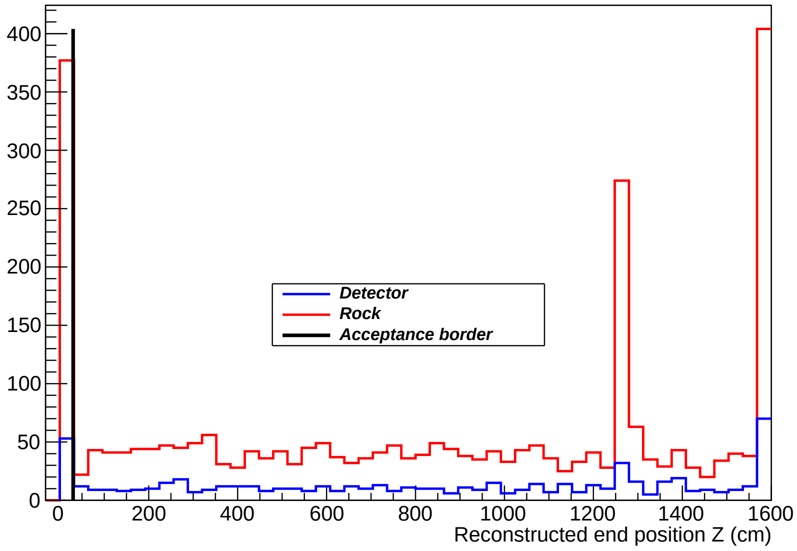

Figure 4.13: The Selection 2 $N-1$ plot of end_z.

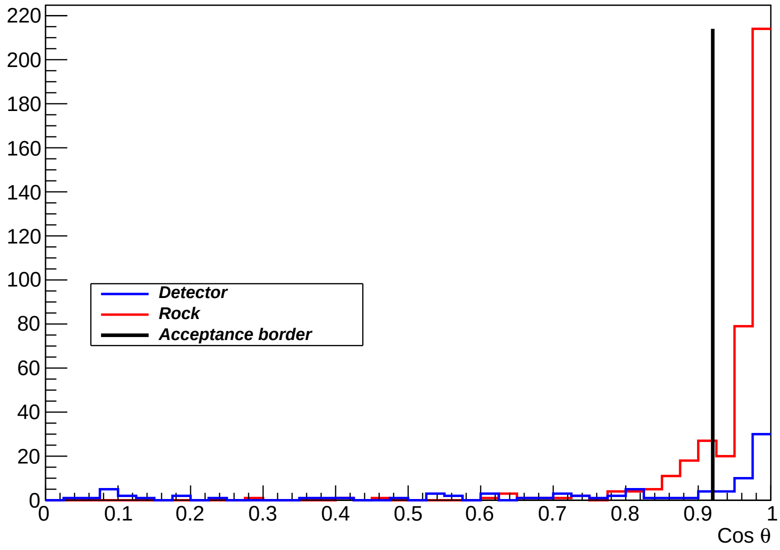

Figure 4.14: The Selection 2 $N-1$ plot of cos θ.

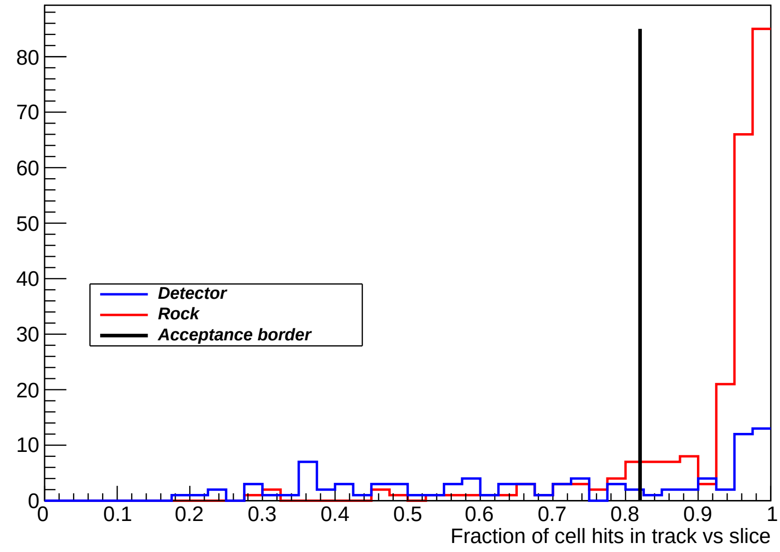

Figure 4.15: The Selection 2 $N-1$ plot of f_{slice}.

4.5.3 Selection 2 Summary

In the Table 4.2 the stats of the Selection 2 are shown. With the 375 misreconstructed rock tracks that passed the criteria out of all the 470 misreconstructed rock tracks in the test data set and with the total of 426 misreconstructed tracks passing the criteria the efficiency and purity values are:

$$\epsilon = 79.8\% \tag{4.6}$$

$$p = 88\% \tag{4.7}$$

To demonstrate the overall effect of the Selection 2 criteria the plot of track lengths after all criteria applied is shown in Fig. 4.16. The prevailance of the rock events is apparent. The coverage of the ND by the Selection 2 tracks is shown in cells vs planes plots Fig. 4.17, x view left and y view right. Again, the missing values are the channels that were deliberately masked off. It's apparent that the recovered upgoing tracks in this selection are covering well the upper part of the detector which couldn't have been reached by the strictly downgoing Selection 1 tracks as can be seen in the y view plot.

Table 4.2: Selection 2 stats.

Total number of misreconstructed tracks in file	715
Total number of misreconstructed rock muon tracks in file	470
Number of misreconstructed Rock tracks that passed the cuts	375
Number of Detector tracks that passed the cuts	51

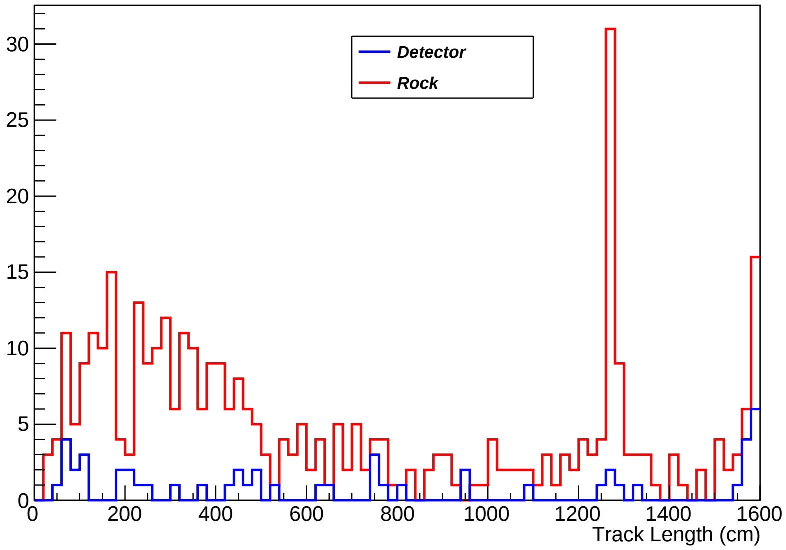

Figure 4.16: The distribution of the track lengths after applying all the Selection 2 criteria. The detector events are below the rock events throughout the whole range.

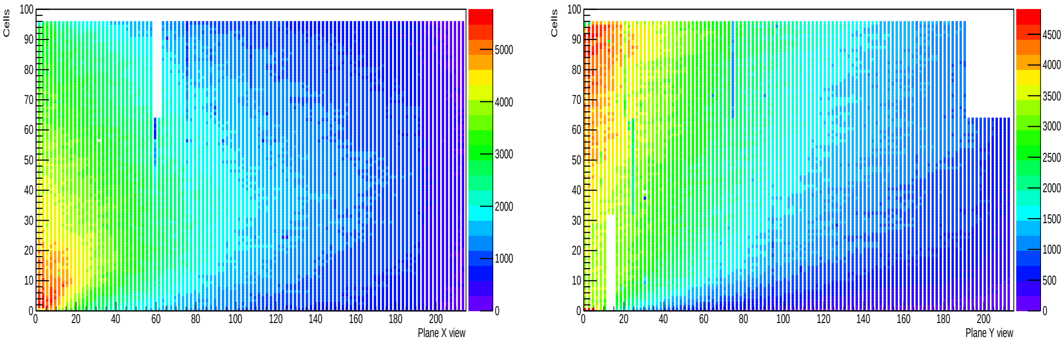

Figure 4.17: The cells vs planes plots representing the coverage of the ND by the Selection 2 sample tracks. **Left**: x view. **Right**: y view. The upward tendency of this sample is visible. Thanks to that the top part of the detector is well covered as can be seen on the y view plot.

.

4.6 The Rock Muon Selection performance

The final Rock Muon Selection is made by combining the Selection 1 and Selection 2 criteria with the 'OR' logical operator. Therefore in the final sample there are tracks that passed either of the two selection criteria sets, ensuring presence of both downgoing as well as recovered upgoing tracks.

In the Table 4.3 the stats of the Rock Muon Selection are shown. With the 1600 rock tracks that passed the criteria out of all the 3645 rock tracks in the test file and with the total of 1777 tracks passing the criteria the efficiency and purity values are:

$$\epsilon = 43.8\% \tag{4.8}$$

$$p = 90\% \tag{4.9}$$

In Fig. 4.18 are the plots of cells vs planes, x view right and y view left. The coverage of the combined sample seems sufficient except for the parts in the very back. Parts of the Muon catcher therefore might not be able to get calibrated by the Rock Muon sample because of the low statistics.

Table 4.3: The Rock Muon Selection stats.

Total number of tracks in file	8543
Total number of rock muon tracks in file	3645
Number of Rock tracks that passed the cuts	1600
Number of Detector tracks that passed the cuts	177

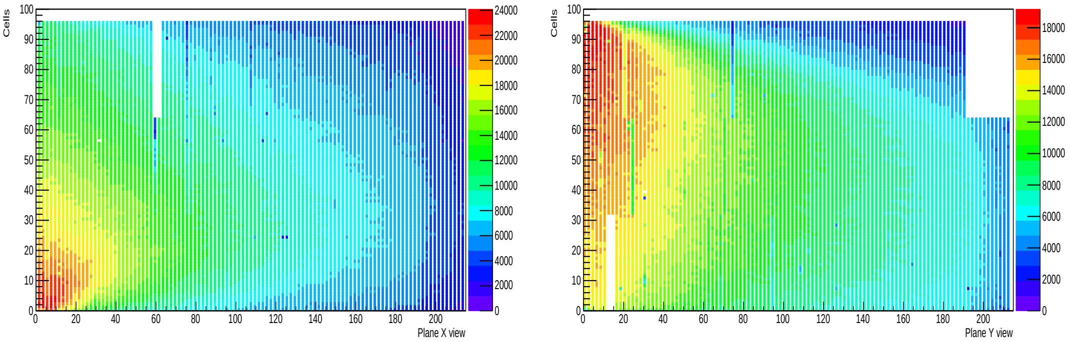

Figure 4.18: The cells vs planes plots representing the coverage of the ND by the final Rock Muon Selection sample tracks. **Left**: x view. **Right**: y view. Thanks to the recovery of misreconstructed upgoing tracks the coverage of the Selection 1 was improved, mainly in the top part of the detector.

.

5. Comparison of the relative calibration using Rock Muons and Cosmic Muons

This section guides through the whole relative calibration process and at each step compares the results from the rock muon sample and the cosmic muon sample. How the rock muon sample was created is discussed in Chapter 4. The cosmic muon sample was created by applying several quality cuts on the files generated using the simulation package CRY as mentioned in Section 2.5.

Specific steps that were studied are following:

- **Uncorrected response per cm $R^{\mathbf{n}}$**, see Section 5.1. Comparison of the raw signal without any corrections applied.
- **Threshold correction**, see Section 5.2. Description of the threshold correction is discussed in Section 3.2.1.
- **Shadowing correction**, see Section 5.3. Description of the shadowing correction is discussed in Section 3.2.2.
- **Combined threshold and shadowing correction**, see Section 5.4. Comparison of the product of threshold and shadowing correction.
- **Corrected response per cm $R^{\mathbf{n}}_{\mathbf{corr}}$**, see Section 5.5. Plots of R^{n} after applying threshold and shadowing corrections.
- **Attenuation calibration fit parameters**, see Section 5.6. Comparison of parameter values from attenuation fits. Description of the attenuation calibration is in Section 3.2.3.

All of the comparison plots in the following sections, except for the last one, are the profile histograms made from 2D distributions of given variables. To construct the profile histograms we used the TProfile class functions in the ROOT framework which calculates the mean of the y values in each bin on x axis.

5.1 Uncorrected response per cm $R^{\mathbf{n}}$

In Fig. 5.1 and Fig. 5.2 are plots of the uncorrected R^{n} vs W for x view and y view, respectively. The distributions have increasing trend towards the positive values of W. The readout is positioned at the positive end of W in each cell. Due to the attenuation effect the further the hit occurred from the readout the lower value of PE will be detected and vice versa. There are also some differences in both views. The inconsistency in the uncorrected R^{n} of cosmic and rock muons seems to stem from different distributions of path lengths both types of muons produce, see Fig. 5.3. Since the rock muons direction is almost perpendicular to the detector they would usually cross the cells along their depth. The rock muons distribution in both views peaks at 6 cm which is the depth of the cell. On the other hand, the cosmic muons enter the detector in different angles from above crossing the vertical cells (x view) along their length (400 cm) and horizontal cells (y view) along their width (4 cm). Because of the variety of angles by which cosmic muons can cross the vertical cells the distribution of path lengths in x view is broad across the whole accepted range. In the case of y view there is a peak at the cell width value 4 cm as expected. It's been observed that R^{n} is not generally constant across the path length values, see Fig. 5.4 showing the R^{n} vs path length in a cell from the ND. The distribution of the uncorrected R^{n} of rock muons is very similar in both views as the path lenghts distributions are also alike. The cosmics uncorrected R^{n} distributions differ as their path length distributions in x and y view differ, too. These distinctnesses at the elementary raw R^{n} level subsequently result in calibration differences in further steps.

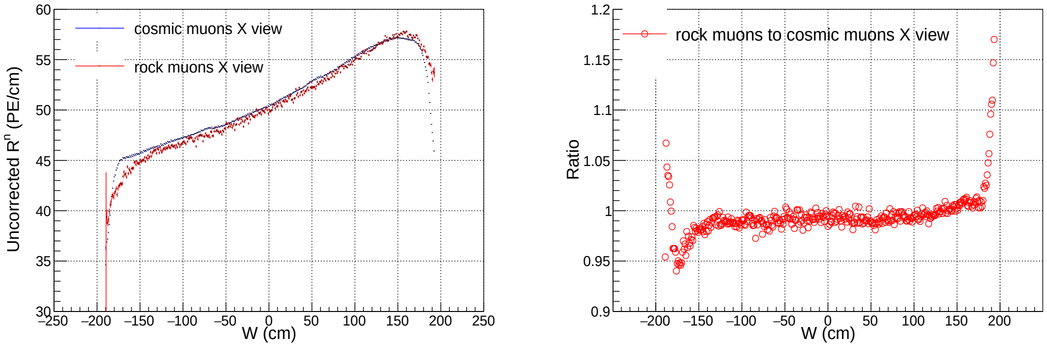

Figure 5.1: **Left:** Plot of the uncorrected R^{n} vs W in x view, comparison of the rock muons (red) and the cosmic muons (blue). The differences seem to stem from different path lengths distributions. **Right:** Ratio of the distributions on left.

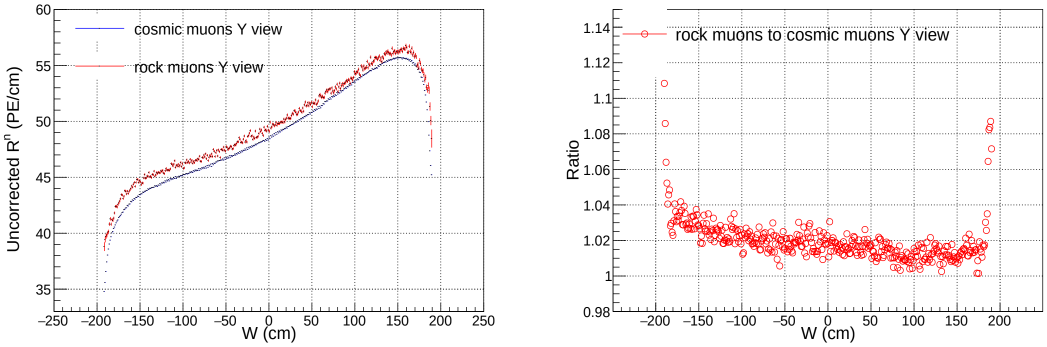

Figure 5.2: **Left:** Plot of the uncorrected R^{n} vs W in y view, comparison of the rock muons (red) and the cosmic muons (blue). The differences seem to stem from different path lengths distributions. **Right:** Ratio of the distributions on left.

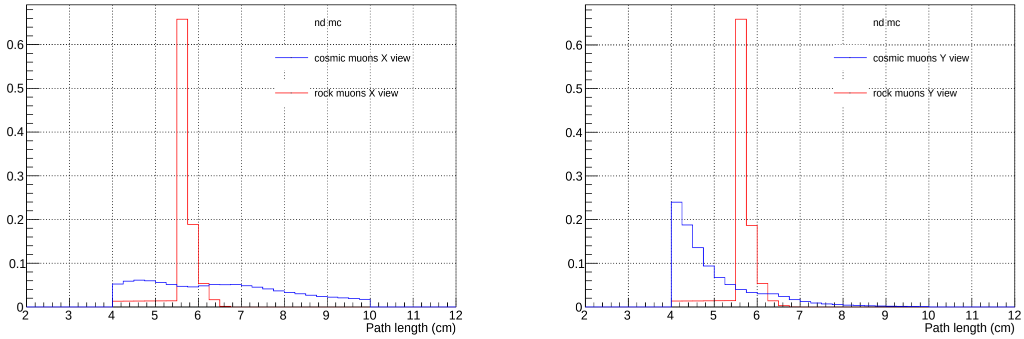

Figure 5.3: Distributions of the cosmic muons (blue) and the rock muons (red) path lengths. **Left:** In x view. **Right:** In y view. The distributions are the same for the rock muons as they cross the cells through the same dimension (6 cm depth) in both views. Cosmic muons cross the vertical cells along their longest dimension therefore the x view distribution is flat. The horizontal cells are crossed along their shortest dimension 4 cm width therefore the distribution peaks at this value in y view. We plot the distributions only of tracks used for the calibration. Selected were tracks with path lengths in cell ranging from 4 cm to 10 cm.

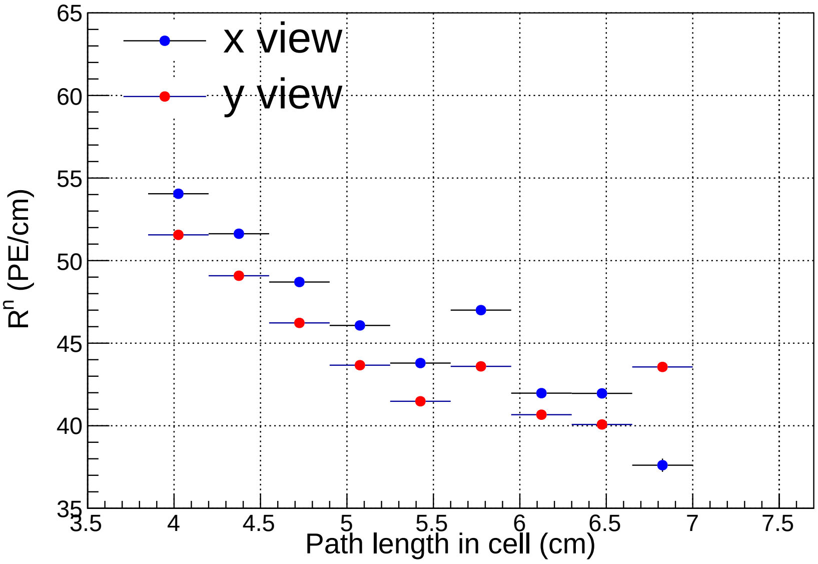

Figure 5.4: Plot of the R^{n} vs path length in a cell for x view (blue) and y view (red) of the rock muon tracks in the ND. The distribution is not constant in either view.

5.2 Threshold correction

The comparison of the threshold correction of cosmic and rock muons is in Fig. 5.5 for x view and Fig. 5.6 for y view. The rock muon threshold correction is nearly constant throughout the whole range for both views. The cosmic muon threshold correction is below the rock and deviates a little from a constant value in both views.

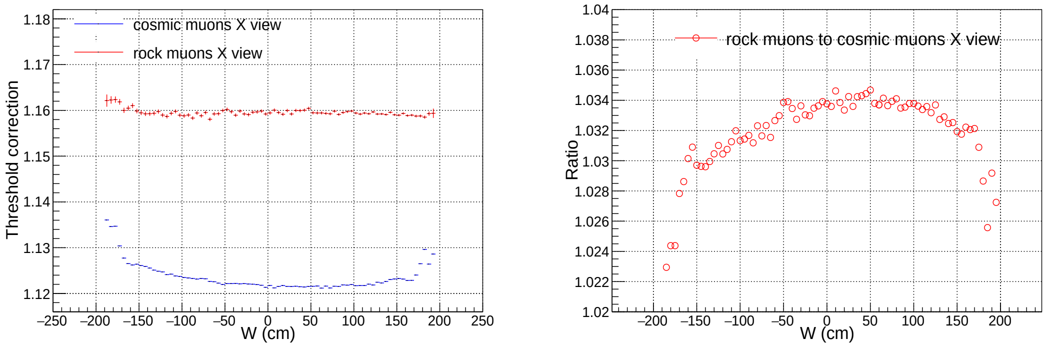

Figure 5.5: **Left:** Plot of the threshold correction vs W in x view, comparison of the rock muons (red) and cosmic muons (blue). **Right:** Ratio of the distributions on left.

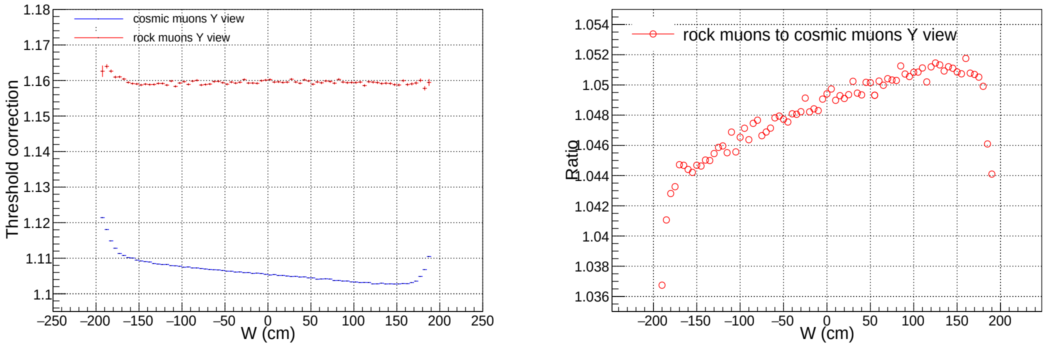

Figure 5.6: **Left:** Plot of the threshold correction vs W in y view, comparison of the rock muons (red) and cosmic muons (blue). **Right:** Ratio of the distributions on left.

The threshold correction is calculated by the Eq. (3.1) as a division of variables R_{mip} and $\lambda_{\mathrm{Poisson}}$. To closely study the structure of the threshold correction it is necessary to look at the distributions of variables it is comprised of. The comparison of the R_{mip} of rock muons and cosmic muons is in Fig. 5.7 for x view and in Fig. 5.8 for y view. The comparison of the $\lambda_{Poisson}$ of rock muons and cosmic muons is in Fig. 5.9 for x view and in Fig. 5.10 for y view. These variables have increasing trend towards the positive values of W such as the uncorrected R^{n} due to the attenuation effect.

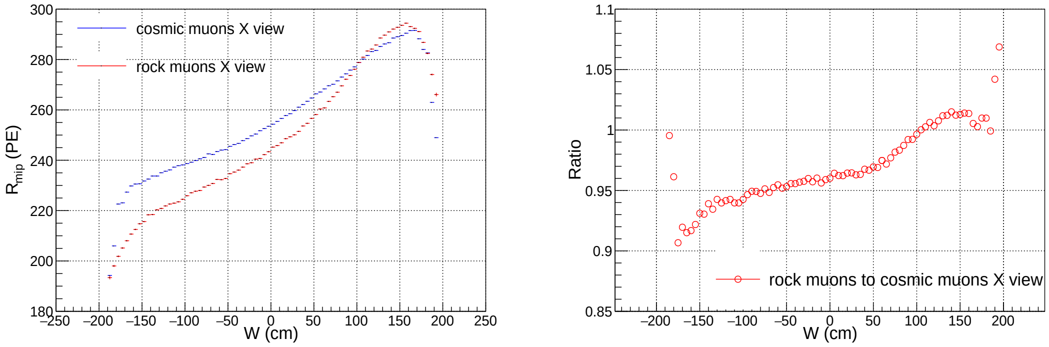

Figure 5.7: **Left:** Plot of the R_{mip} vs W in x view, comparison of rock muons (red) and cosmic muons (blue). **Right:** Ratio of the distributions on left.

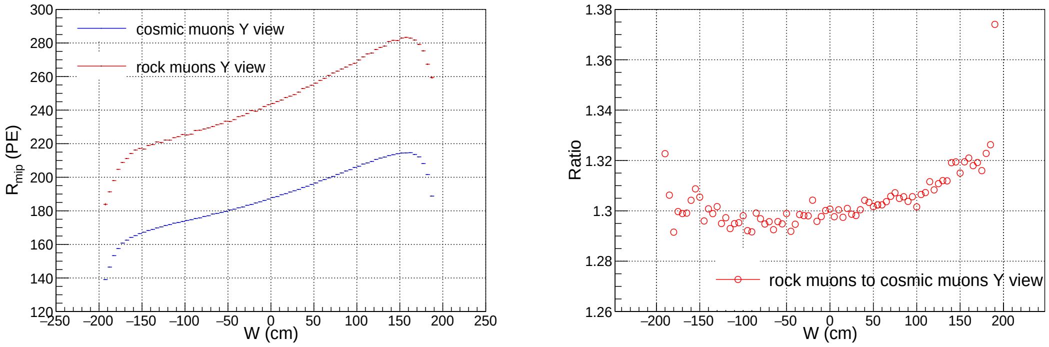

Figure 5.8: **Left:** Plot of the R_{mip} vs W in y view, comparison of rock muons (red) and cosmic muons (blue). **Right:** Ratio of the distributions on left.

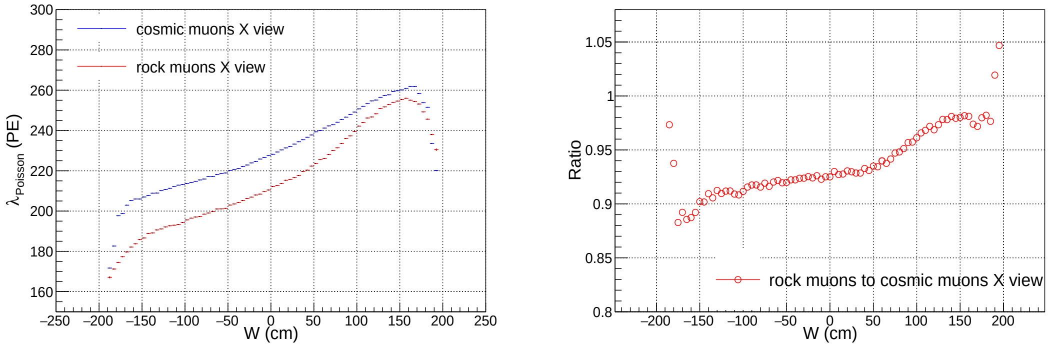

Figure 5.9: **Left:** Plot of the $\lambda_{\mathrm{Poisson}}$ vs W in x view, comparison of rock muons (red) and cosmic muons (blue). **Right:** Ratio of the distributions on left.

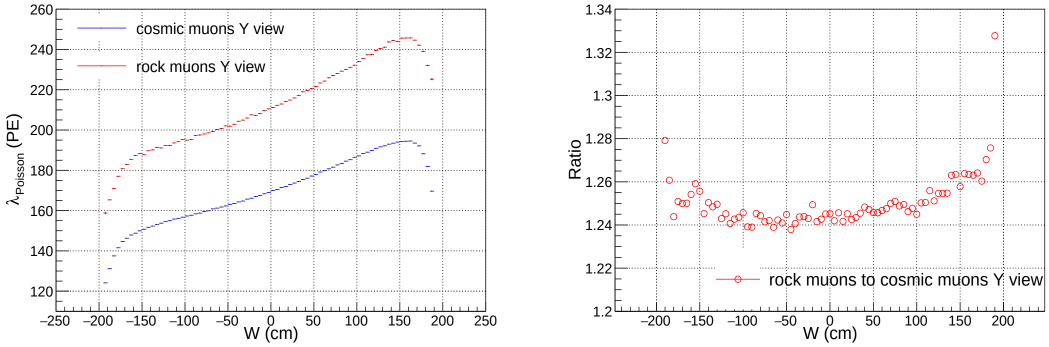

Figure 5.10: **Left:** Plot of the λ_{Poisson} vs W in y view, comparison of rock muons (red) and cosmic muons (blue). **Right:** Ratio of the distributions on left.

5.3 Shadowing correction

The comparison of the shadowing correction of cosmic and rock muons is in Fig. 5.11 for x view and Fig. 5.12 for y view. The rock and cosmic shadowing corrections are nearly constant in the y view. In the x view both cosmic and rock corrections start to decline from around the W value of 50 cm.

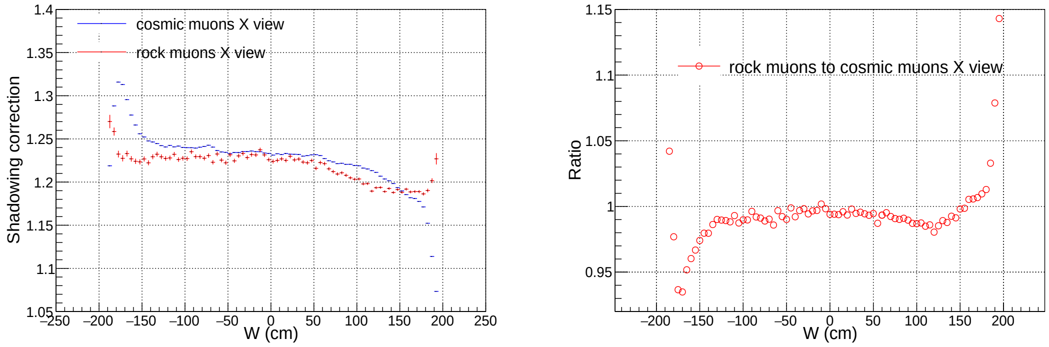

Figure 5.11: **Left:** Plot of the shadowing correction vs W in x view, comparison of rock muons (red) and cosmic muons (blue). **Right:** Ratio of the distributions on left.

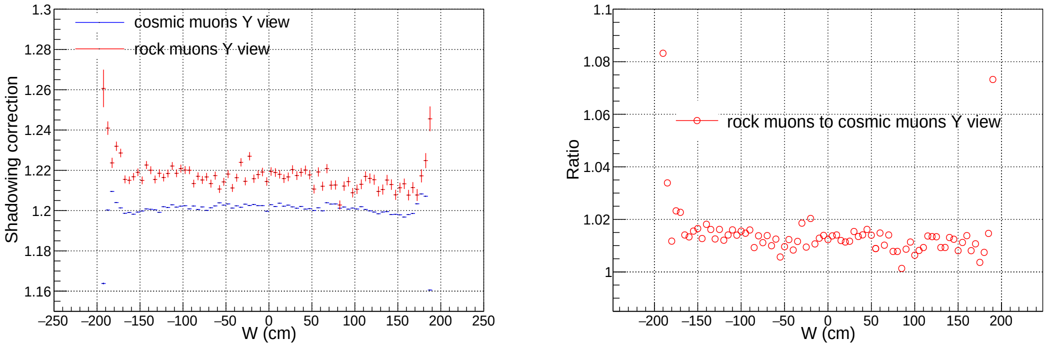

Figure 5.12: **Left:** Plot of the shadowing correction vs W in y view, comparison of rock muons (red) and cosmic muons (blue). **Right:** Ratio of the distributions on left.

The shadowing correction is calculated by the Eq. (3.3) as a division of variables E_{true} and E_{mip}. To explain the behaviour of the shadowing correction it is necessary to look at the distributions of variables it is comprised of. The comparison of the E_{true} of rock muons and cosmic muons is in Fig. 5.13 for x view and in Fig. 5.14 for y view. The comparison of the E_{mip} of rock muons and cosmic muons is in Fig. 5.15 for x view and in Fig. 5.16 for y view. Since the distribution of the cosmic E_{mip} in x view is nearly constant the only factor adding to the decrease of the cosmic shadowing correction is the E_{true} variable. The cosmic muons entering from above in mostly vertical directions deposit more energy at the ends of their tracks which are usually positioned at the lower parts of the vertical cells. These are the parts of the negative W where the E_{true} variable shows higher values than in the positive W parts as expected. In the rock muon plots of E_{true} and E_{mip} in the x view we can see a bump at the positive side of the W coordinate. The source of the bump roots from the method the plots were made. The original 2D histograms of the variables are in Fig. 5.17. The structure of the histograms in the parts of the positive W values is different from the rest of the plot. The distributions tail there doesn't follow the gaussian behaviour which results in skewed mean evaluation, off the distributions peak, creating the bump in profile histograms. Since also the structure of both 2D histograms is different, the division of their profiles gives not constant results as we can see on the former shadowing correction in Fig. 5.11.

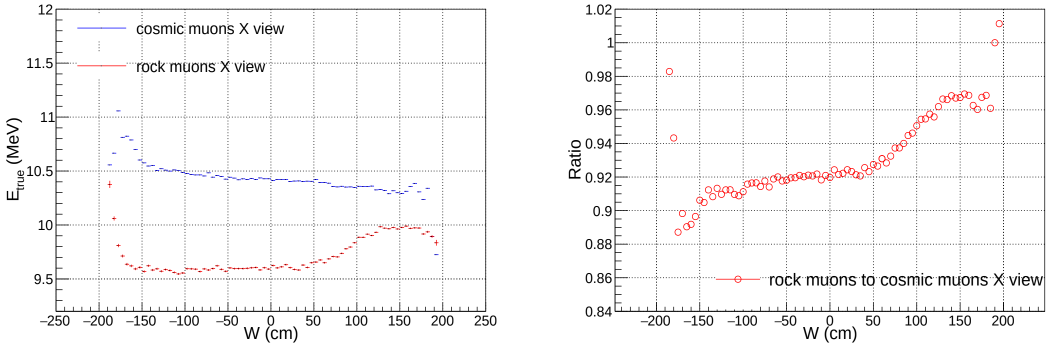

Figure 5.13: **Left:** Plot of E_{true} in MeV vs W in x view, comparison of rock muons (red) and cosmic muons (blue). **Right:** Ratio of the distributions on left.

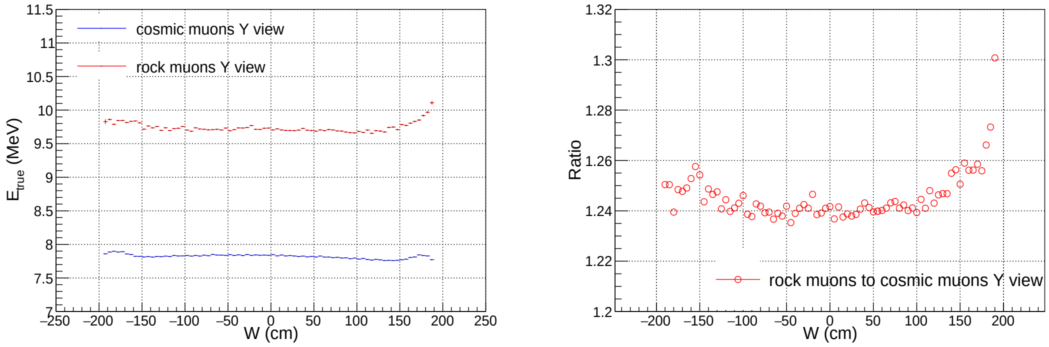

Figure 5.14: **Left:** Plot of E_{true} in MeV vs W in y view, comparison of rock muons (red) and cosmic muons (blue). **Right:** Ratio of the distributions on left.

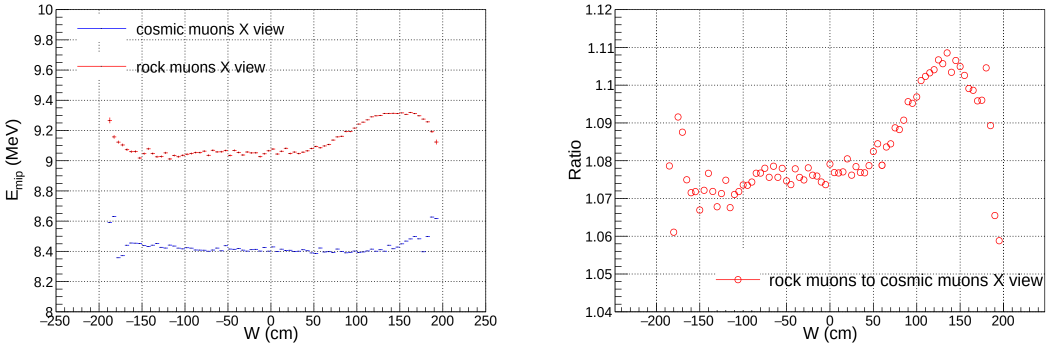

Figure 5.15: **Left:** Plot of E_{mip} vs W in x view, comparison of rock muons (red) and cosmic muons (blue). **Right:** Ratio of the distributions on left.

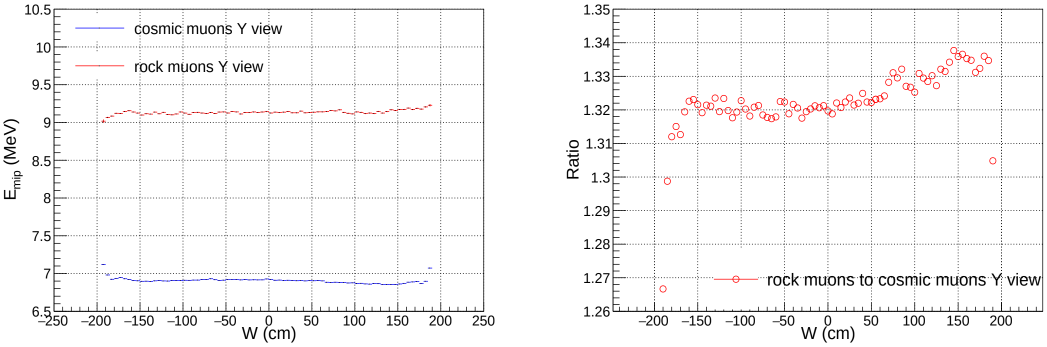

Figure 5.16: **Left:** Plot of E_{mip} vs W in y view, comparison of rock muons (red) and cosmic muons (blue). **Right:** Ratio of the distributions on left.

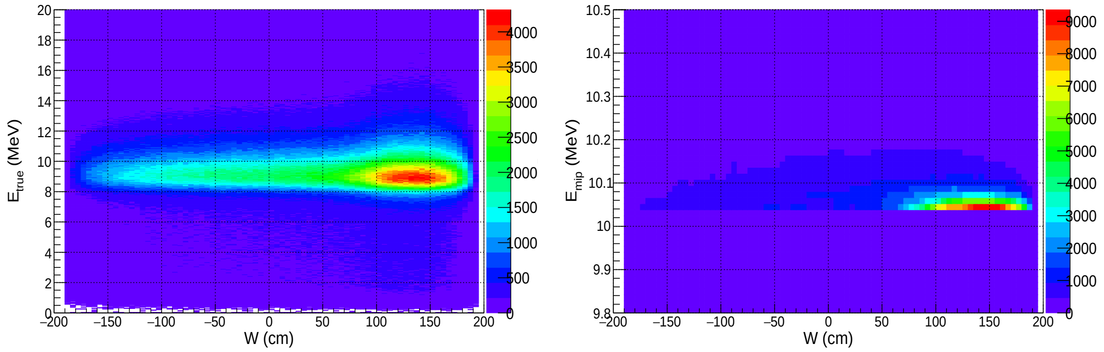

Figure 5.17: 2D histograms of variables comprising the rock muon shadow correction vs W in x view. **Left:** A 2D histogram of the rock muon E_{true} in MeV vs W in x view. **Right:** A 2D histogram of the rock muon E_{mip} vs W in x view. Both distributions have considerably more hits at the positive side of the W coordinate. That is, in the upper part of the detector. This is in agreement with the y view cells vs planes plot on fig. 4.18 right where we see that the detector gets the most hits in the higher positioned cells.

5.4 Combined threshold and shadowing correction

By multiplying the threshold and shadowing corrections the combined correction is obtained. That is then being applied to the uncorrected R^{n} to obtain the corrected $R^{\mathrm{n}}_{\mathrm{corr}}$. Comparison of the combined threshold and shadowing corrections of rock and cosmic muons is in Fig. 5.18 for x view and in Fig. 5.19 for y view.

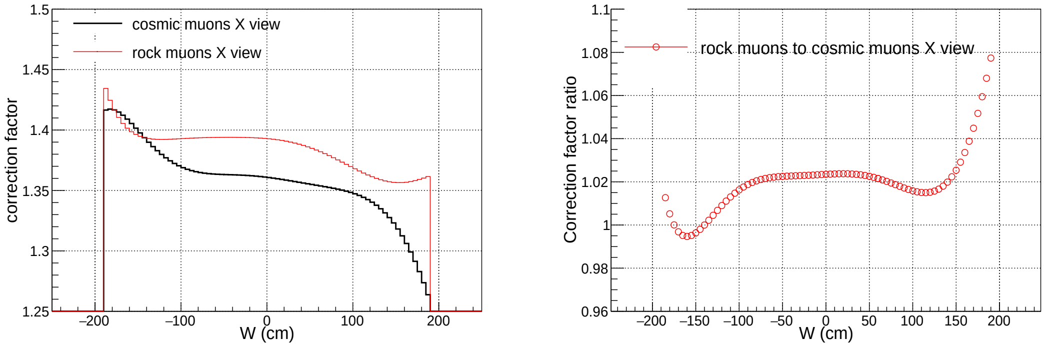

Figure 5.18: **Left:** Plot of the combined threshold and shadowing correction vs W in x view, comparison of rock muons (red) and cosmic muons (black). **Right:** Ratio of the distributions on left.

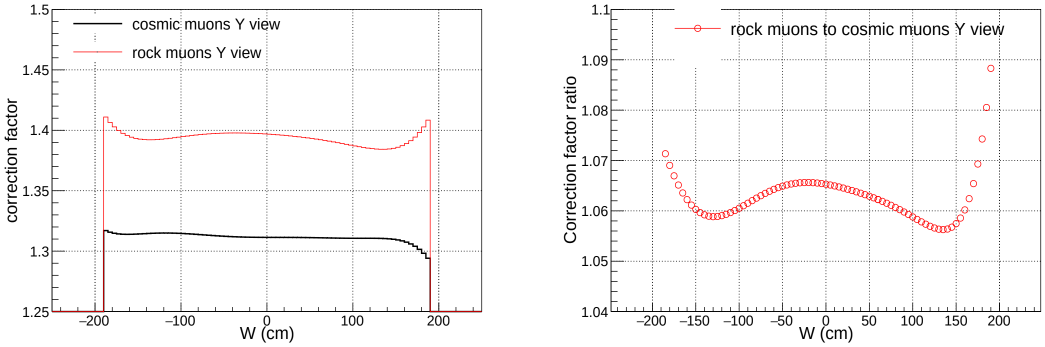

Figure 5.19: **Left:** Plot of the combined threshold and shadowing correction vs W in y view, comparison of rock muons (red) and cosmic muons (black). **Right:** Ratio of the distributions on left.

5.5 Corrected response per cm $R^{\mathrm{n}}_{\mathrm{corr}}$

After applying the combined threshold and shadowing correction on the uncorrected R^{n} values the $R^{\mathrm{n}}_{\mathrm{corr}}$ values are obtained. The $R^{\mathrm{n}}_{\mathrm{corr}}$ vs W comparison plot of rock and cosmic muons is in Fig. 5.20 for x view and in Fig. 5.21 for y view. The uncorrected R^{n} distribution of the rock muons in Fig. 5.1 was almost overlaying the cosmic distribution in x view while in y view in Fig. 5.2 the rock values were slightly above the cosmic values. The applied correction unified the mutual rock and cosmic values positions with rock being now moderately below the cosmic values in both views. The increasing trend towards the positive W values due to the attenuation effect was preserved. In the next step the attenuation calibration is performed to correct for this phenomenon.

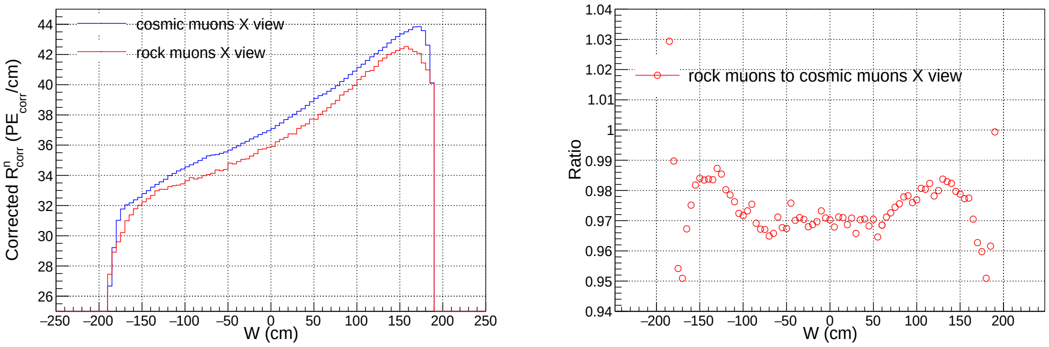

Figure 5.20: **Left:** Plot of the $R^{\mathrm{n}}_{\mathrm{corr}}$ vs W in x view, comparison of rock muons (red) and cosmic muons (blue). **Right:** Ratio of the distributions on left.

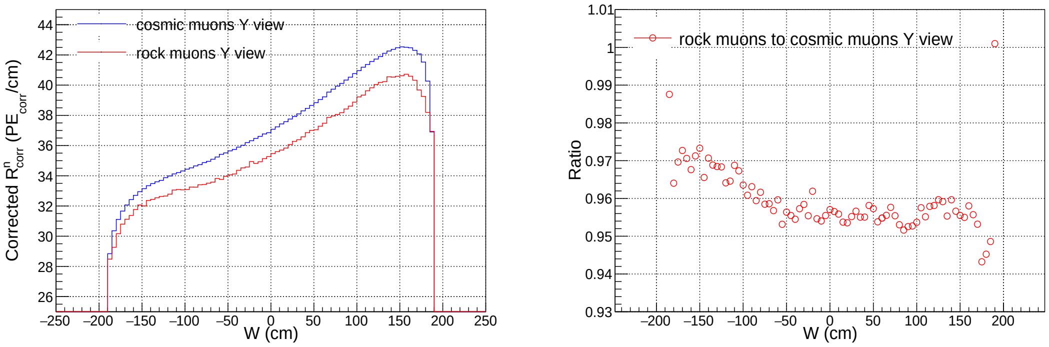

Figure 5.21: **Left:** Plot of the $R^{\mathrm{n}}_{\mathrm{corr}}$ vs W in y view, comparison of rock muons (red) and cosmic muons (blue). **Right:** Ratio of the distributions on left.

5.6 Attenuation fit parameters

In each channel the $R^{\mathrm{n}}_{\mathrm{corr}}$ vs W histograms are fit to a double exponential function Eq. (3.7) with parameters C (background), X (attenuation length) and A (scaling factor) as described in Section 3.2.3. The parameter values which are the results of the fit are presented in this section. To compare cosmic and rock parameter values the following metric was calculated for each parameter:

$$\frac{\Delta\text{parameter}}{\text{parameter}} = \frac{\text{rock parameter value} - \text{cosmic parameter value}}{\text{rock parameter value}}, \qquad (5.1)$$

where parameter $= C, X, A$. Values for this metric were filled into histograms from all channels shown left in the following plots. Plots on the right are 2D histograms of rock parameter vs cosmic parameter values demonstrating the correlation between them. Left plots are peaking at zero and right plots show the linear relationship between the rock and cosmic parameters. This indicates that the usage of rock and cosmic muons for the calibration gives similar results. The variable plots are in Fig. 5.22, Fig. 5.23 and Fig. 5.24. For each fit the χ^2 is calculated. If a channel has a value of $\chi^2 < 0.2$ it is marked as calibrated, otherwise it is considered as not calibrated. The χ^2 plots are in Fig. 5.25. In Table 5.1 are counts of channels having $\chi^2 < 0.2$ calibrated using rock and cosmic muons. The cosmic muon calibration covers well the whole ND. The rock muons calibrated only 199 of 352 cells. All the uncalibrated cells are from the Muon catcher from which only 7 vertical cells got calibrated with the rest of it being uncalibrated. The example of the calibrated and uncalibrated cell is in Fig. 5.26. In the uncalibrated example the rock muon data points are scattered with no evident structure and have big error bars. It is a result of low statistics as not many muon tracks make it to and through the Muon catcher. Also, there is only a limited number of simulated rock muon tracks being repeated in the files so using more files wouldn't add more rock muon tracks which could improve the statistics.

Table 5.1: Number of calibrated channels using rock vs cosmic muons

	Rock	Cosmic
calibrated channels	199	352
$\chi^2 < 0.2$	(56.5%)	(100%)

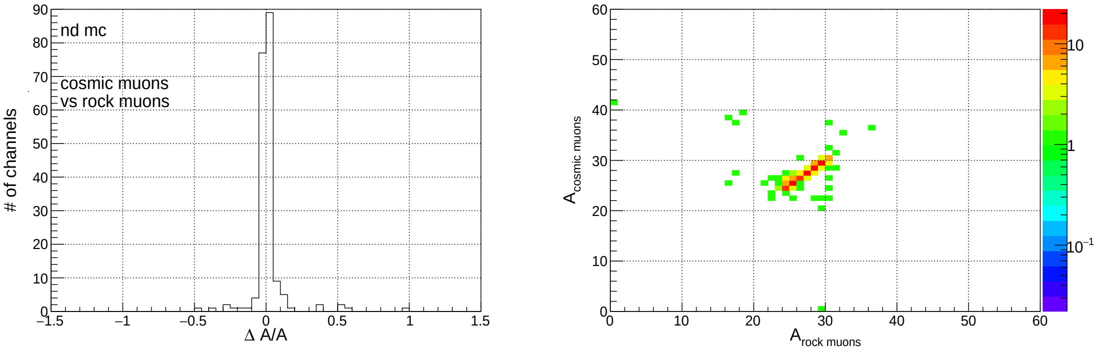

Figure 5.22: **Left:** Plot of $\frac{\Delta A}{A}$ calculated by Eq. (5.1). Peak around zero shows the value of this parameter is similar for cosmic and rock muon calibration. **Right:** Values of A parameter of rock muons vs cosmic muons. Linear correlation confirms the similarity between both.

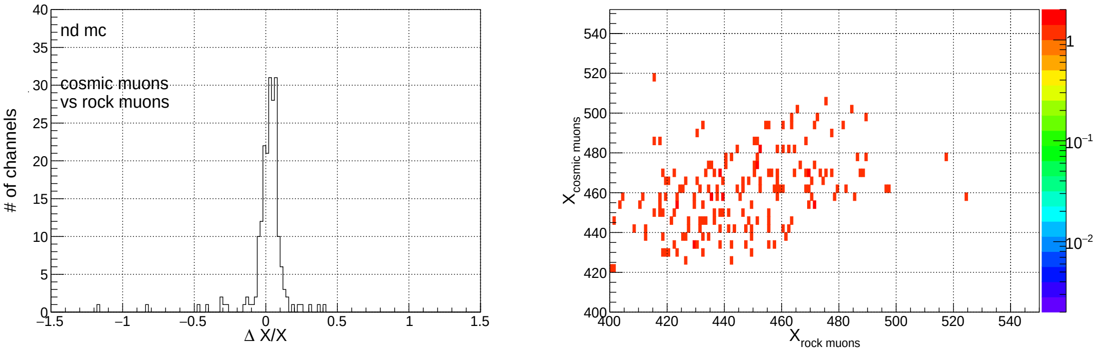

Figure 5.23: **Left:** Plot of $\frac{\Delta X}{X}$ calculated by Eq. (5.1). Peak around zero shows the value of this parameter is similar for cosmic and rock muon calibration. **Right:** Values of X parameter of rock muons vs cosmic muons. Linear correlation confirms the similarity between both.

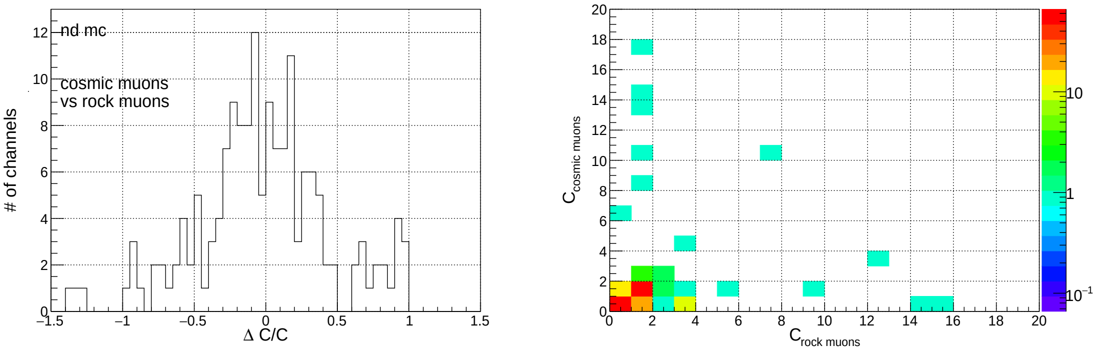

Figure 5.24: **Left:** Plot of $\frac{\Delta C}{C}$ calculated by Eq. (5.1). Peak around zero shows the value of this parameter is similar for cosmic and rock muon calibration. **Right:** Values of C parameter of rock muons vs cosmic muons. Linear correlation confirms the similarity between both.

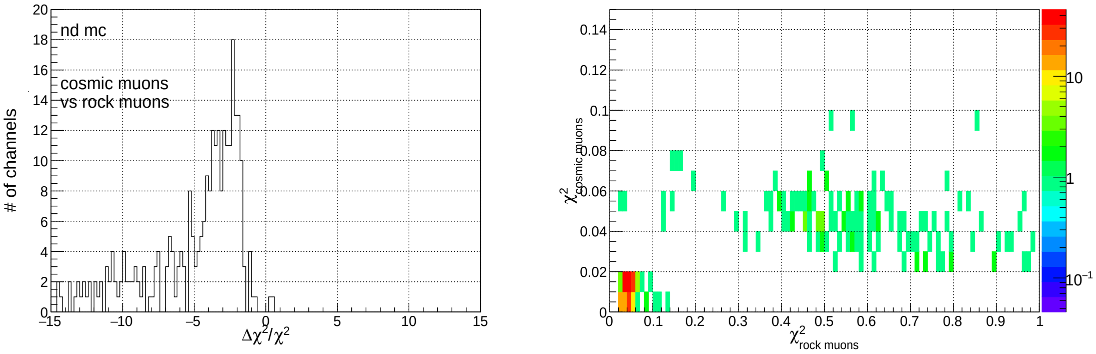

Figure 5.25: **Left:** Plot of $\frac{\Delta(\chi^2)}{\chi^2}$ calculated by Eq. (5.1). Values of cosmic and rock χ^2 are different as many rock channels couldn't be fit with the double exponential and have values of χ^2 higher than 0.2 **Right:** χ^2 of rock muons vs cosmic muons. All cosmic channels have $\chi^2 < 0.2$ and calibrated is thus the whole detector. Many rock channels have $\chi^2 > 0.2$ and couldn't be calibrated. All rock uncalibrated channels are from the Muon catcher.

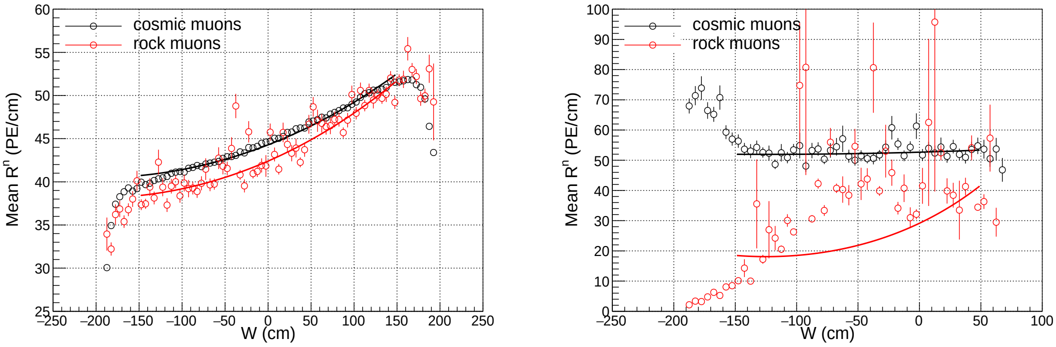

Figure 5.26: Examples of two cells — one with successful and the other with unsuccessful rock muon attenuation fit. Fit function is indicated with full line. **Left:** Vertical cell number 3 in the active region of the ND got successfully calibrated by both rock muons and cosmic muons. The attenuation fit resulted with the $\chi^2 < 0.2$ in both cases. **Right:** Vertical cell number 25 in the Muon catcher got successfully calibrated only by the cosmic muons. The attenuation fit of the rock muon values resulted with the $\chi^2 > 0.2$. We can see from the plot that rock muon values are irregularly scattered with big error bars indicating poor statistics in this cell.

Conclusion

We described the calibration process of the NOνA experiment detectors with a special focus on the relative calibration. The relative calibration consists of 3 main parts: threshold, shadowing and attenuation calibration.

In the individual steps we compared the performance of two muon samples: cosmic muons which are standardly used and rock muons as an alternative and independent source. First, the selection criteria to prepare the sample of rock muons were developed. This was done by studying various reconstructed variables. Three variables were chosen on which were then made constraints: reconstructed start position, cos θ and f_{slice}. The resulting rock muon sample reached the efficiency and purity as follows: $\epsilon = 43.8\%$, $p = 90\%$. With this sample the comparisons between the rock muons and cosmic muons in terms of variables entering the relative calibration were made. The initial difference between the two samples stemmed in their different path length in cell distributions due to the different directions in which they enter the ND. It was discovered that the uncorrected R^{n} is not constant across a range of path lengths in cell and that resulted in the inconsistencies at the uncorrected R^{n} level. Nevertheless, the attenuation calibration fit parameters were well correlated between the cosmic and rock muon samples. This fact confirms the validity of the current calibration process with cosmic muons. The only disadvantage of the rock muons appeared to be the low number of their simulated tracks. Due to this circumstance not enough rock muons made it to the Muon catcher and therefore it ended poorly calibrated. Cosmic muons have much greater coverage and calibrate the whole detector well.

The next step would be to use the real data to avoid low rock muons number of simulated tracks as well as to see the comparison between the simulated and real data calibration.

References

[1] S. M. Bilenky. *Neutrino. History of a unique particle.* 2012, arXiv: 1210.3065v1

[2] C. L. Cowan, F. Reines, F. B. Harrison, H. W. Kruse and A. D. McGuire. Detection of the Free Neutrino: A Confirmation. *Science*, 1956, doi:10.1126/science.124.3212.103.

[3] B. Pontecorvo. *Mesonium and antimesonium.* Sov. Phys. JETP, 6, 429, 1957.

[4] K. A. Olive et al. (Particle Data Group), Chin. Phys. C, 38, 090001 (2016).

[5] M. Maki, M. Nakagawa, S. Sakata. *Remarks on the unified model of elementary particles.* Prog. Theor. Phys. 28,870(1962).

[6] C. Giunti. *No Effect of Majorana Phases in Neutrino Oscillations.* arXiv:1001.0760, 2010.

[7] K. Zuber. *Neutrino Physics.* Series in High Energy Physics, Cosmology and Gravitation Series. Taylor & Francis, 2004.

[8] M. D. Baird. *An analysis of muon neutrino disappearance from the NUMI beam using an optimal track fitter.* 2015, `http://lss.fnal.gov/archive/thesis/2000/fermilab-thesis-2015-24.pdf`, 2017/04/16.

[9] G. Brunetti. *New Results from NOvA.* 2016, `http://nova-docdb.fnal.gov/cgi-bin/RetrieveFile?docid=16275&filename=PSI2016_NOvA.pdf&version=4`, 2017/04/16.

[10] F. P. An et al. (Daya Bay Collab.), Phys. Rev. Lett. 115, 111802 (2015).

[11] M. V. Diwan,V. Galymov, X. Qian, and A. Rubbia. *Long-Baseline Neutrino Experiments.* arXiv:1608.06237, 2016.

[12] J. A. Thomas,P. L. Vahle. *Neutrino oscillations: Present Status and Future Plans.* World Scientific, 2008.

[13] E. Niner. *Observation of electron neutrino appearance in the NuMI beam with the NOvA experiment.* 2015, `http://lss.fnal.gov/archive/thesis/2000/fermilab-thesis-2015-16.pdf`, 2017/04/16.

[14] Carlo Giunti and Chung W. Kim. *Fundamentals of Neutrino Physics and Astrophysics.* Oxford University Press, 2007.

[15] L. Kolupaeva, O. Samoylov, I. Shandrov. *Matter effect in neutrino oscillations for NOvA experiment.* 2016, `http://nova-docdb.fnal.gov/cgi-bin/RetrieveFile?docid=14985&filename=AYSS.pdf&version=3`, 2017/04/16.

[16] K. Sachdev. *Muon Neutrino to Electron Neutrino Oscillation in NOvA*. 2015, `https://inspirehep.net/record/1391605/files/fermilab-thesis-2015-20.pdf`, 2017/04/16.

[17] D. S. Ayres et al.. The nova technical design report. Technical report, Fermilab, Batavia, Illinois, 2007.

[18] S. M. Lein. *Muon Neutrino Contained Disappearance in NOvA*. 2015, `http://inspirehep.net/record/1391606/files/fermilab-thesis-2015-21.pdf`, 2017/04/16.

[19] M. Betancourt. *Study of Quasi-Elastic Scattering in the NOvA Detector Prototype*. 2013, `http://lss.fnal.gov/archive/thesis/2000/fermilab-thesis-2013-10.pdf`, 2017/04/16.

[20] B. Rebel. *Window Tracking Algorithm for Cosmic Rays*. Unpublised NOvA internal document 2014.

[21] A. Aurisano. *The NOvA Detector Simulation*. Unpublished NOvA internal document 2015.

[22] T. Bohlen. *The FLUKA Code: Developments and Challenges for High Energy and Medical Applications*. Nucl. Data Sheets 120, 211 (2014).

[23] A. Ferrari, P. R. Sala, A. Fasso, and J. Ranft. *FLUKA: A multiparticle transport code (Program version 2005)*. Technical Report CERN-2005-010 CERN 2005.

[24] M. Campanella, A. Ferrari, P. Sala, and S. Vanini. *First Calorimeter Simulation with the FLUGG Prototype*. Technical Report CERN-ATL-SOFT-99-004 CERN 1999.

[25] C. Andreopoulos et al. *The GENIE Neutrino Monte Carlo Generator*. Nucl. Instrum. Meth. A614, 87 (2010).

[26] C. Hagmann, D, Lange, D. Wright. *Cosmic-ray shower generator (CRY) for Monte Carlo transport codes*. Nuclear Science Symp. Conf. Rec. (Honolulu, HI) volume 2, pages 1143-1146 IEEE 2007.

[27] S. Agostinelli et al. *Geant4 - A Simulation Toolkit*. Nucl. Instrum. Meth. A506, 250 (2003).

[28] J. Allison et al. *Geant4 Developments and Applications*. IEE Trans. Nucl. Sci. 53, 270 (2006).

[29] C. Backhouse, A. Radovic, P. Singh. *The Attenuation and Threshold Calibration of the NOvA detectors*. Unpublished NOvA internal document 2016.

List of Figures

List of Tables